Passive Gust Alleviation for a Flying Wing Aircraft

Dr. Shijun Guo
Prof. Otto Sensburg

Cranfield University
College Rd
Cranfield, Bedford MK43 0AL
United Kingdom

Report Date: January 2013

Final Report from 26 August 2011 to 24 November 2012

Air Force Research Laboratory
Air Force Office of Scientific Research
European Office of Aerospace Research and Development
Unit 4515 Box 14, APO AE 09421

REPORT DOCUMENTATION PAGE

Form Approved OMB No. 0704-0188

1. REPORT DATE *(DD-MM-YYYY)*	2. REPORT TYPE	3. DATES COVERED *(From – To)*
10 January 2013	Final Report	26 August 2011 – 24 November 2012

4. TITLE AND SUBTITLE	5a. CONTRACT NUMBER
Passive Gust Alleviation for a Flying Wing Aircraft	**FA8655-11-1-3073**
	5b. GRANT NUMBER
	Grant 11-3073
	5c. PROGRAM ELEMENT NUMBER
	61102F

6. AUTHOR(S)	5d. PROJECT NUMBER
Dr. Shijun Guo	
Prof. Otto Sensburg	**5d. TASK NUMBER**
	5e. WORK UNIT NUMBER

7. PERFORMING ORGANIZATION NAME(S) AND ADDRESS(ES)	8. PERFORMING ORGANIZATION REPORT NUMBER
Cranfield University College Rd Cranfield, Bedford MK43 0AL United Kingdom	N/A

9. SPONSORING/MONITORING AGENCY NAME(S) AND ADDRESS(ES)	10. SPONSOR/MONITOR'S ACRONYM(S)
EOARD Unit 4515 BOX 14 APO AE 09421	AFRL/AFOSR/IOE (EOARD)
	11. SPONSOR/MONITOR'S REPORT NUMBER(S)
	AFRL-AFOSR-UK-TR-2013-0008

12. DISTRIBUTION/AVAILABILITY STATEMENT

Distribution A: Approved for public release; distribution is unlimited.

13. SUPPLEMENTARY NOTES

14. ABSTRACT

This final report presents the work and results of a research project 'Passive Gust Alleviation for a Flying Wing Aircraft' funded by EOARD/US AFRL (Contract FA8655-11-1-8073) from 26 Aug. 2011 to 24 Nov. 2012. In the project, an investigation was made into the technology potential of a passive gust alleviation device (PGAD) and its application to a Sensorcraft of high aspect ratio in flying wing configuration. It is aimed at minimizing the gust response of the aircraft by using the PGAD integrated at the wing tip. The project has been carried out in four stages: the loading analysis including aerodynamic calculation and mass estimation, structural design and modeling, gust response analysis and optimal design of the PGAD for minimum gust response.

15. SUBJECT TERMS

EOARD, gust alleviation, flying wing aircraft

16. SECURITY CLASSIFICATION OF:			17. LIMITATION OF ABSTRACT	18. NUMBER OF PAGES	19a. NAME OF RESPONSIBLE PERSON
a. REPORT UNCLAS	**b. ABSTRACT** UNCLAS	**c. THIS PAGE** UNCLAS	SAR	90	Gregg Abate
					19b. TELEPHONE NUMBER *(Include area code)* +44 (0)1895 616021

Standard Form 298 (Rev. 8/98)
Prescribed by ANSI Std. Z39-18

Final Technical Report:

(FA8655-11-1-3073)

Passive Gust Alleviation for a Flying Wing Aircraft

Dr Shijun Guo

Prof. Otto Sensburg

Aerospace Engineering

Cranfield University, UK

10. Jan. 2013

EXECUTIVE SUMMARY

This final report presents the work and results of a research project 'Passive Gust Alleviation for a Flying Wing Aircraft' funded by EOARD/US AFRL (Contract FA8655-11-1-8073) from 26 Aug. 2011 to 24 Nov. 2012. In the project, an investigation was made into the technology potential of a passive gust alleviation device (PGAD) and its application to a Sensorcraft of high aspect ratio in flying wing configuration. It is aimed at minimizing the gust response of the aircraft by using the PGAD integrated at the wing tip. The project has been carried out in four stages: the loading analysis including aerodynamic calculation and mass estimation, structural design and modeling, gust response analysis and optimal design of the PGAD for minimum gust response.

In the aerodynamic analysis, different methods including vortex lattice and CFD methods were employed and used to calculate the loading at specified flight cases. In the preliminary design phase, mass distribution was estimated based on the MTOW of 55 tones and primary systems including the structures, airframe systems, power plant, fuel, avionics and landing gears. From these data, the shear force, bending moment and torque diagrams acting on the structure were calculated.

In the initial layout of the structure, a conventional configuration was selected with consideration of the PGAD at the wing tip. The skin panels are reinforced by I-section stringers to resist buckling. The wing is mainly made of carbon/epoxy composites. Structural design including stiffened panel buckling and stress analysis was carried out by using the FE method to make sure the large sweep and high aspect wing structure meets the design requirements. The initial sizing of the major components was based on the strength and buckling criteria. The initial design of the aircraft structure was followed by detailed stress analysis by using the NASTRAN finite element method. The results show that the failure indices are below one and the strains below 3600 $\mu\varepsilon$ under limit load. The elastic deflection of the wing at semi-span 31.6 m wing tip

reaches 2.4 m under limit load in the worst case. The flutter speed of 241 m/s and frequency 6.2 Hz for the full fuel case was predicted for the aircraft.

With a maximum weight and a span of 63 m, the sensitivity of the wing to the gust is a major concern. Subsequently modal analysis and gust response of the wing to a discrete (1-cos) gust load in a range of equivalent frequencies were calculated. The gust model is in compliance with the EASA CS-25 airworthiness requirement. Two flight cases of zero-fuel and full-fuel mass at sea level were considered. Without the PGAD, the gust response amplitude at wing tip reaches approximately 4 m for the worst full-fuel case at sea level.

Finally the gust response was evaluated by taking the PGAD with optimized key design parameters subject to normal flight constraints. The optimized PGAD together with the wing aeroelastic effects is very effective. For the case where rigid-body motion is constrained and PGAD twist angle is limited to 10 degree, the gust response in terms of wing tip deflection and wing root bending moment can be reduced by over 18% and 15% respectively. When the transverse rigid-body motion is set free with the PGAD twist angle limited to 10 degree, the gust response in terms of wing elastic deflection and bending moment can be reduced by over 20% and 17% respectively.

ACKNOWLEDGMENTS

TABLE OF CONTENTS

1. Introduction

This project is aimed at minimizing the gust response of a flying wing aircraft by using a passive gust alleviation device (PGAD) mounted at the wing tip. Although various passive gust alleviation technology has been proposed and investigated in previous research [1-2] especially for similar type of sensorcraft [3-10], this proposed PGAD concept presents an effective option. The concept of PGAD is illustrated in Fig.1a where a separate rigid wing section called PGAD is mounted to the wing tip through an elastic hinge. The elastic hinge is made of a torque spring and a rotation shaft, which is mounted to the front spar and end rib of the wing and the PGAD as illustrated in Fig.1a. By setting the rotation shaft axis in front of the aerodynamic center, the PGAD will twist nose down in response to a gust load to alleviate the aerodynamic force. As illustrated in Fig.1b, the gust induced wing load distribution over the wing would be significantly reduced by employing the PGAD. For this particular aircraft of a large sweep back wing, the wing bending-torsion coupling and aeroelastic effect will also contribute to the gust alleviation. As the results, it can minimize the negative impact of gust on the airframe and flight performance.
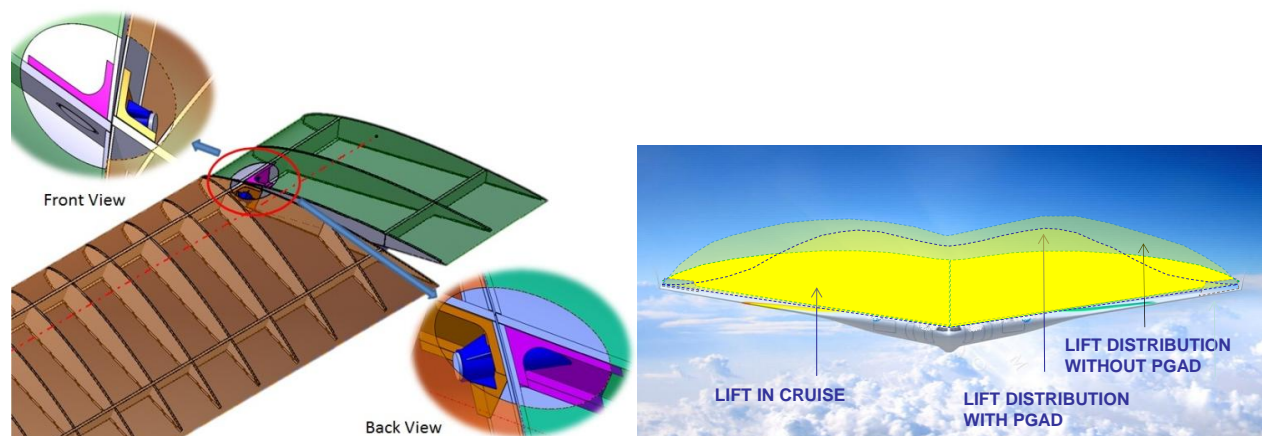

Figure 1. (a) PGAD at wing tip, (b) Lift distribution with and without PGAD

The nose down rotation of the PGAD surface is a self-induced passive motion in response to an increase of aerodynamic force such as gust load. The effectiveness of the PGAD depends upon the

1

key design parameters and the wing dynamic behavior. The composite wing can be tailored by optimizing the wing structure. The primary PGAD design parameters are the torque spring stiffness, position of the shaft attachment and dimension of the device. The torque spring stiffness and position of the shaft attachment determine the twist angle, quantity of gust alleviation and how fast the PGAD reacts. The dimension of the device scales the amount of gust response alleviation but is limited by the flight performance in normal load condition. The surface area on the device in front of the axis "feels" the gust first and tries to move the device nose-up in a very short period, but soon the whole device will then rotate nose down with the load alleviated.

To develop and evaluate the PGAD technology, a research proposal was made and a 15-month contract was granted by EOARD/AFRL. In the proposal, a work programme and time schedule as shown in Table 1 was set for the project.

Table 1. Work Programme and Time Schedule

Work Package		Activity	Elapsed Time [months]
1.		Original flying wing	
	1.1.	Data collection and FE modelling of the original wing structure using Patran / Nastran package	2
	1.2.	Fully stressed wing structure analysis under 2.5g limit load and 3.75g ultimate load for a valid wing box design.	1
	1.3.	Vibration, flutter and divergence analysis of the baseline design	1.5
	1.4.	Tuned gust stress analysis for initial evaluation of the baseline design.	1
2.		Wing model with gust alleviation device.	
	2.1.	Initial analysis to determine an optimal dimension, torsion spring stiffness and location for a tuned gust under the design constraint	1.5
	2.2.	Analysis of the whole wing with an optimal passively rotating section for maximum gust alleviation including aeroelastic effect	1.5
	2.3.	FE model of the wing structure with an integrated gust alleviation device – an optimal design of a passively rotating wing tip section for a tuned gust	1.5
	2.4.	Vibration, flutter and divergence analysis	1
	2.5.	Tuned gust stress analysis at wing root to evaluate the device	1
3.		Wing model with soft wing tip.	
	3.1.	Determine optimal thickness and material (laminate layup) for the tip section	0.5
	3.2.	Tuned gust stress analysis.	0.5
	3.3.	Vibration, flutter and divergence analysis.	1
4.		Final technical report.	1
		Total:	**15 months**

A large aircraft of MTOW 55 tones with a high aspect ratio wing span 63 m and flying wing configuration is taken in the case study. The project has been carried out in four stages started from the loading analysis including aerodynamic calculation and mass estimation and followed by structure design and analysis, dynamic and gust response analysis and optimal design of the PGAD for minimum gust response.

In the Report Chapter 2, the aerodynamic analysis results by vortex lattice and CFD methods in specified flight cases were presented. The aircraft mass distribution was estimated based on the MTOW and primary systems including the structures, airframe systems, power plant, fuel, avionics and landing gears. From these data, the shear force, bending moment and torque diagrams acting on the structure were calculated and presented.

In Chapter 3, the theoretical base for analytical analysis of the aircraft structure was presented first. The structure initial layout in a conventional configuration was selected with the PGAD at the wing tip. Structural design including stiffened panel buckling and stress analysis was carried out based on the theory. The initial design of the aircraft structure was followed by detailed stress analysis by using NASTRAN finite element method to make sure the structure meet the design requirements. The results show that the failure indices are below one and the strains below 3600 $\mu\varepsilon$ under ultimate load. The wing tip deflection of the wing of semi-span 31.6 m reaches 2.4 m under limit load in the worst case.

In Chapter 4, modal analysis to assess the structure dynamic behavior was carried out followed by gust response analysis of the wing to a discrete (1-cos) gust load in a range of equivalent frequency were calculated. The gust model is in compliance with the EASA CS-25 airworthiness. Two flight cases in zero-fuel mass and full-fuel mass at sea level were considered. Without the PGAD, the gust response amplitude at wing tip reaches approximately 4 m for the full-fuel case at sea level.

Finally the gust response was evaluated by taking the PGAD with optimized key design parameters subject to normal flight constraint. The optimized PGAD together with the wing aeroelastic effect is very effective. When rigid-body motion is constrained, the gust response in

terms of pure elastic deflection of the wing and maximum bending moment can be reduced by over 18% and 15% respectively with the PGAD twist angle limited to 10 degree. When the transverse rigid-body motion is set free with the same PGAD twist angle limit, the gust response in terms of wing elastic deflection and bending moment have been reduced by over 20% and 17% respectively.

2.   Aircraft Load Analysis

2.1   Aircraft data and aerodynamic load

The aircraft basic data given is listed in Table 2. The geometry data is shown in Figure A1 in Appendix A. The cruise speed is M=0.65 at altitude 18.3 km. The flight speed for critical gust load is M=0.3 at sea level. Without the detailed wing airfoil data, a standard NACA4415 is chosen because of its best match with the available geometry.

Table 2. Design technical data of the aircraft

Wing semi span (m)	Fuselage length (m)	MTOM (full fuel, kg)	MTOM (empty fuel, kg)	Sweep angle (deg)	Cruise altitude, km
31.6	14.7	55350	27674	30	18.3

The aerodynamic pressure and load distribution over the 3D whole aircraft was calculated by using CFD method. The flow velocity and vortex plot from the CFD simulation as shown in Fig.3 shows the source of the pressure drop in the aircraft body-wing kink region and the wing tip. The aerodynamic force at different angle of attack (AoA) was calculated by CFD method. Through the analysis, the results show that the lifting force at AoA=5 degree meets the lift requirement in full fuel MTOM case at cruise M=0.65. The method is also compared with vortex lattice method, panel method and lifting line theory with the spanwise lifting force distribution results shown in Fig.4. From the results, it is noted that the 3D effect of wing on the lift distribution along the span especially the outer wing captured by the CFD method is more significant than the other methods.

4
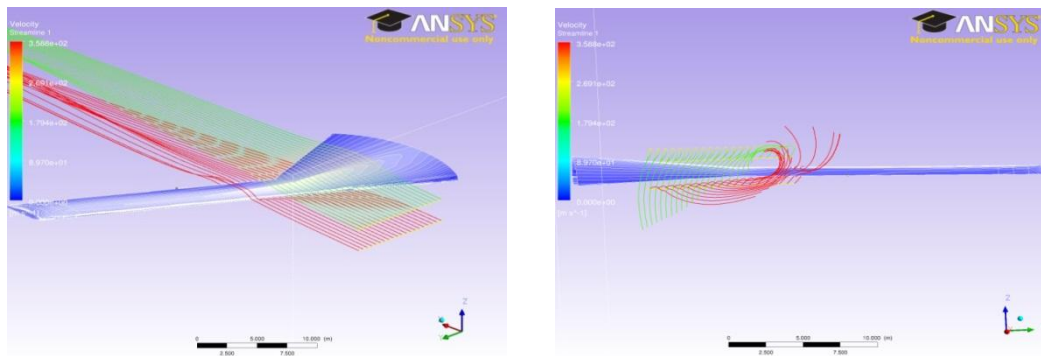
Figure 3. Flow velocity and vortex effect on the pressure at the wing kink region

<table>
<tr><td>(a)</td><td>(b)</td></tr>
</table>
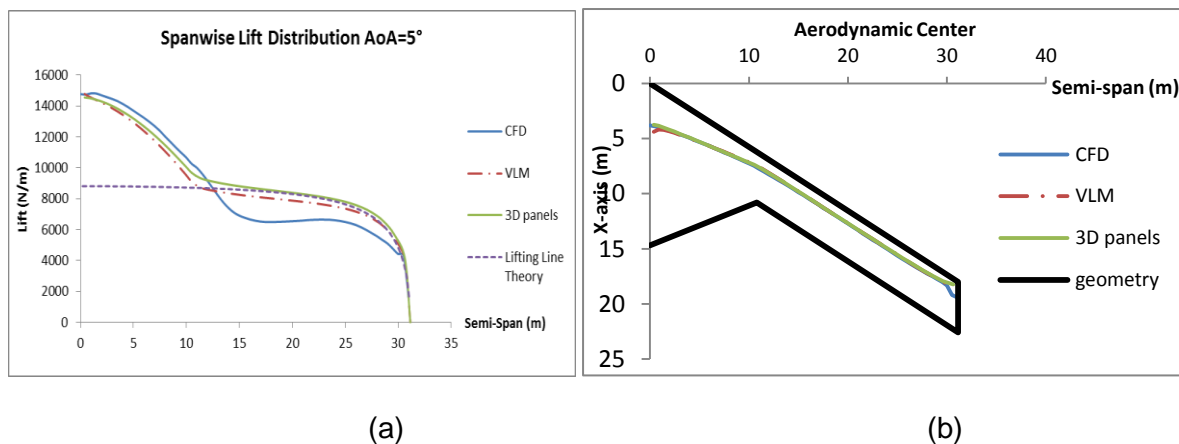
Figure 4. (a) Spanwise lifting force and (b) aerodynamic centre by different methods

2.2 Aircraft mass estimation

The aircraft mass distribution was estimated based on the MTOW and primary systems including the structures, airframe systems, power plant, fuel, avionics and landing gears. Three fuel tanks are located in the wing box as shown in Fig.5. The mass and location of the engine and landing gears are also shown in Fig.5. The system mass is also considered in the example.

Mass distribution for half aircraft structures is 5700 kg, the power plant and landing gears are 2500 kg, systems 3500 kg and full fuel 15900 kg in the loading evaluation. Detailed mass estimation is presented in Appendix B. The resulting shear force and bending moment distribution along the span is calculated and shown in Fig.6.

5
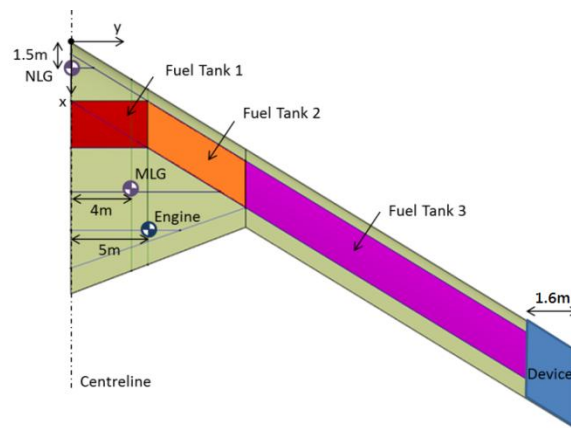
Figure 5.   Half aircraft with location of fuel tanks, engine and LG
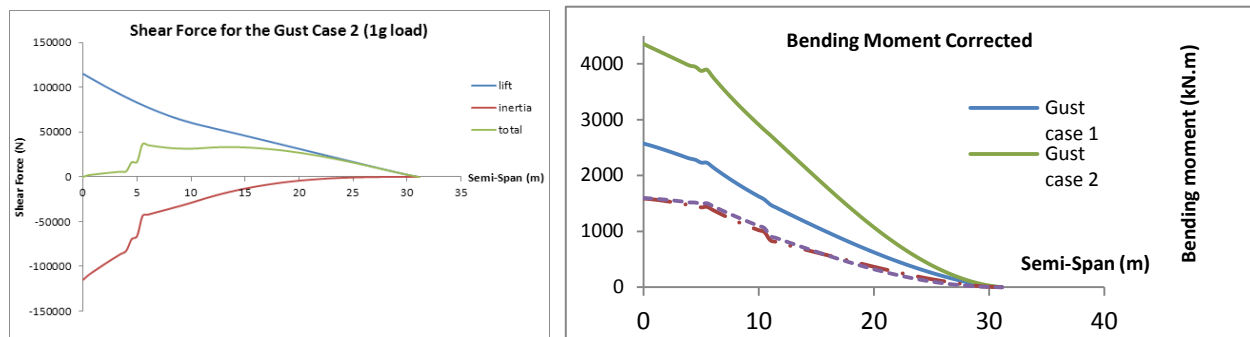
Figure 6. (a) Shear force and (b) bending moment diagram in different cases

3.   Analytical and Numerical Methods

3.1   Theoretical study

3.1.1   The theory and analytical method

Since no structure details were available, an initial structure analysis was carried out based on the calculated load shown in Chapter 2. In the initial design stage, the structural model was simplified to a thin-walled composite beam model. The method developed by Armanios and Badir [14] and the dynamic stiffness method [15] were used and described below. In the stiffness modeling of a wing box, the wing was divided into 20 spanwise segments with each one modeled as a uniform thin-walled double-cell box beam between the leading edge and rear spar. The whole

6

wing structure was modeled as an assembly of those box beams along the span. A relationship between the bending moment *Mx*, torque *My* and the transverse and twist deflections at the end of an anisotropic thin-walled closed-section beam are expressed below.

$$M_y = C_{22}\phi' + C_{23}h'' \quad \text{and} \quad M_x = C_{23}\phi' + C_{33}h'' \tag{1}$$

The stiffness coefficients *Cij* of each segment can be calculated based on its geometry and material properties and integration along its cross sectional circumference,

$$\left. \begin{array}{ll} C_{22} = \dfrac{A_e^2}{\oint(1/C(s))ds} & C_{23} = -A_e \dfrac{\oint(B(s)/C(s))z\,ds}{\oint(1/C(s))ds} \\[4mm] C_{33} = \oint\left(A(s) - \dfrac{B(s)^2}{C(s)}\right)z^2 ds + \dfrac{\left[\oint(B(s)/C(s))z\,ds\right]^2}{\oint(1/C(s))ds} \end{array} \right\} \tag{2}$$

where A_e is the enclosed area of the cross section; $A(s), B(s)$ and $C(s)$ are given below.

$$A(s) = A_{11} - \frac{(A_{12})^2}{A_{22}}, \quad B(s) = 2\left(A_{16} - \frac{A_{12}A_{26}}{A_{22}}\right), \quad C(s) = 4\left[A_{66} - \frac{(A_{26})^2}{A_{22}}\right] \tag{3}$$

In the above equations, A_{ij} is the coefficients of stiffness matrix (**A**) of the composite skin and spar webs of the closed-section beam. According to the force-deflection relationships in Eq. 1 and stiffness definition, the stiffness coefficients C_{33}, C_{22} and C_{23} actually represent the bending, torsion and bending-torsion coupling rigidities of the wing box beam, which are usually expressed by symbols *EI, GJ* and *CK* respectively. Contribution of the six stringers to the wing box bending stiffness is also included in the model.

The dynamic stiffness matrix method [15] was subsequently used for the dynamic analysis. In this method, the equations of motion for each of the thin-walled box beams were represented as follows, where the bending-torsion stiffness coupling was included but the transverse shear deformation and warping effect were neglected.

$$EI \cdot h'''' + CK \cdot \phi''' + m \cdot \ddot{h} - m \cdot X_\alpha \cdot \ddot{\phi} = 0 \tag{4}$$

$$GJ \cdot \phi'' + CK \cdot h''' + m \cdot X_\alpha \cdot \ddot{h} - I_p \cdot \ddot{\phi} = 0 \tag{5}$$

where $h'''' = \partial^4 h / \partial y^4$, $\ddot{h} = \partial^2 h / \partial t^2$, $\phi''' = \partial^3 h / \partial y^3$ and $\ddot{\phi} = \partial^2 h / \partial t^2$. By solving the differential equations, an exact solution for the displacement function $h(y)$ and $\phi(y)$ can be obtained. A dynamic stiffness matrix for a box beam can be subsequently created by relating the displacements to the bending moment and torque at both ends of the beam. A dynamic stiffness matrix for the whole wing box structure is obtained by assembling all the wing box beam stiffness matrices along the wing span direction.

3.1.2   Gust response analysis

It is noted that the dynamic stiffness matrix is actually a combination of stiffness and mass matrices of the beam and is frequency dependent. Since this particular type of matrix produces a non-standard eigenvalue problem, it is solved by using the Wittrick-William algorithm [16]. By employing the normal mode method, the aeroelastic equation for a wing coupled with shelf excited unsteady aerodynamic forces can be written in generalized coordinates as follows. The unsteady aerodynamic forces were calculated by using the classical Theordorsen theory [17,18] and the strip method in incompressible airflow.

$$\left[[K_D(\omega)] - \frac{1}{2}\rho V^2 [AL]_R + i\omega[D] + i\frac{1}{2}\rho V^2 [AL]_I \right]\{q\} = 0 \tag{6}$$

With gust load as external unsteady aerodynamic force, the aeroelastic response equation of the wing structure is written as

$$[M]\{\ddot{x}\} + [D]\{\dot{x}\} + [K]\{x\} = [AL_1]\{\ddot{x}\} + [AL_2]\{\dot{x}\} + [AL_3]\{x\} + \{AL_{ext}\} \tag{7}$$

where $[M]$, $[D]$, $[K]$ are the structural mass, damping and stiffness matrices; $[AL_i]$ and $[AL_{ext}]$ are the unsteady aerodynamic and external dynamic force matrices respectively. The 1-*cosine* discrete

gust model specified in the airworthiness regulation is used in this current investigation. The gust velocity profile of a 1-cosine model is expressed as below.

$$U = \frac{U_{de}}{2} \times [1 - \cos\left(\frac{\pi s}{H}\right)] \tag{8}$$

where U_{de} is a specified design gust velocity, s is the distance penetrated in the gust, and H is gust gradient distance which is the distance parallel to the airplane's flight path for the gust to reach its peak velocity.

3.1.3   Optimization Method

In the optimization process, the gradient based determinant method (GBDM) used in previous work [19] is employed to determine the PGAD design variables. Effort is primarily focused on minimizing the gust response and loading on the wing. The optimization analysis can be expressed as follows:

$$\text{Minimise } F(x) = \left[1 - \frac{R_{g0} - R_g(x)}{R_{g0}}\right]^2 \tag{9}$$

$$x \in \left\{A\left(K_1, K_2, \ldots d_1, d_2 \ldots\right)\right\} \tag{10}$$

where $F(x)$ is the objective function, $R_g(x)$ wing gust response, x a vector containing the key parameters of the PGAD as design variables.

3.2   Structural layout and initial analysis

The layout of the primary structure of the flying wing aircraft is illustrated in Figure 7. The structure is divided into 11 spanwise sections in the modeling. A multi-spar configuration was chosen for the inner wing and a conventional two-spar configuration for the outer wing. For the inner wing, the front, middle and rear spars are located at 14%, 50%, and 80% wing chord. For the outer wing, the front spar and the rear spar are respectively located at 15% and 75% of the chord at the wing tip and kept parallel to the leading edge along the span.
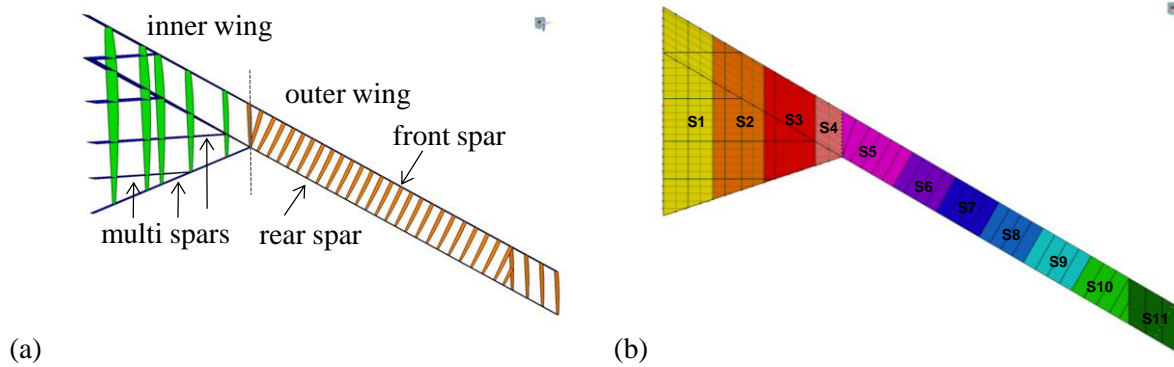
Figure 7. (a) Structural layout and (b) sections of the flying wing aircraft

An intermediate modulus carbon fiber epoxy matrix composite (8552 epoxy matrix IM7 UD carbon fiber) has been chosen for the wing structure. The properties of the material are presented in the Table 3. Based on the loading and structural layout, an initial structural design of the spars, ribs and skin covers was carried out. The results of the initial design of the skin panels in quasi-isotropic layup are listed in Table 4.

Table 3. Some technical Data for aircraft design and layout

E_1 (GPa)	E_2 (GPa)	G (GPa)	v	X_t (MPa)	X_c (MPa)	Y_t (MPa)	Y_c (MPa)	S (MPa)	ρ (kg/m^3)
164	12	5.3	0.32	2724	1690	111	246	120	1570

Table 4. Skin panel thickness of the initial design

Section	Upper skin thickness (mm)	Lower skin thickness (mm)	Section	Upper skin thickness (mm)	Lower skin thickness (mm)
1	4.5	3.7	7	5.2	3.4
2	5.3	2.9	8	4.7	3.9
3	6.0	3.1	9	4.2	3.4
4	7.6	5.2	10	3.1	2.6
5	6.3	4.5	11	2.1	2.9
6	5.8	3.9			

Prier to the FE modeling, the buckling analysis method [11,12] under practical design constraint [13] has been used in the stiffened skin panel design. In the composite structure analysis, the stress level was limited to 3500 micro strain under damage tolerance constraint. Based on the FE model of the structure, which satisfies the buckling and strength requirements,

10

modal analysis and initial dynamic response to a discrete gust input in a range of frequency was conducted without considering aeroelastic effect.

Based on the initial design, a buckling analysis for the stiffened composite skin panels is carried out [11-13]. As an example result, the detailed dimensions of the upper stringer-skin panel in the kink section 5 where the maximum compression load occurs are given in Fig.8. The calculated stringer pitch is 230 mm. The buckling load factors of wing box upper surface panels are checked with ESDU 03001 [13]. The overall and local buckling load factors for this panel are 2.1 and 1.1 respectively.


```
--------   SKIN-STRINGER PANEL SIZING RESULTS   --------
Stringer Base Flange    ba = 35.21 mm      ta = 4.40 mm
Stringer Web            bw = 68.40 mm      tw = 3.42 mm
Stringer Top Flange     bf = 27.36 mm      tf = 3.42 mm
Stringer Cross-section Area       Ast  = 717.68 mm^2
Skin Cross-section Area           Ask  = 1435.36 mm^2
Stringer Spacing                  Pitch = 228.27 mm
```
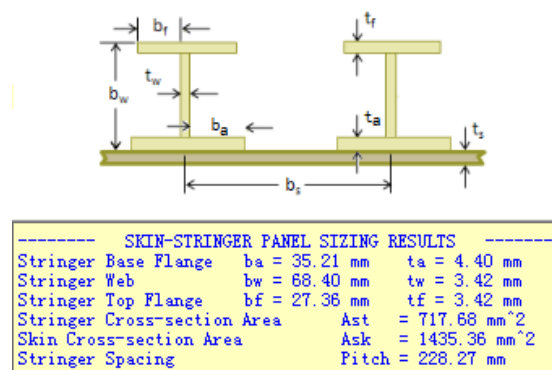
Figure 8. Detailed dimensions of the stringer-skin panel at the critical section 5

3.3   Structural FE model and stress analysis

In this investigation, detailed structural stress and dynamic analysis of the wing structure made of spars, ribs and stringer reinforced skins was carried out by using the FE method based NASTRAN package. In the FE model, the skin, ribs and spar webs are modeled by using shell elements; the stringers and spar capes are modeled as beam element. In the dynamic and gust response analysis, the engine, LG, fuel tanks and control devices and systems were modeled as concentrated mass located at the center of gravity of the components.

The FE analysis results show a maximum displacement of 2.56 m at the wing tip under limit load (2.5g). The associated failure index (FI) of the upper skin is under 0.51 as shown in Fig. 9(a). The maximum strain magnitude reaches 3320 με which is under the limit of 3600 με as shown in

Fig. 9(b). It can be observed that the critical strain and stress are located around the kink where the stress concentration occurs due to wing geometric change.

(a)   (b)
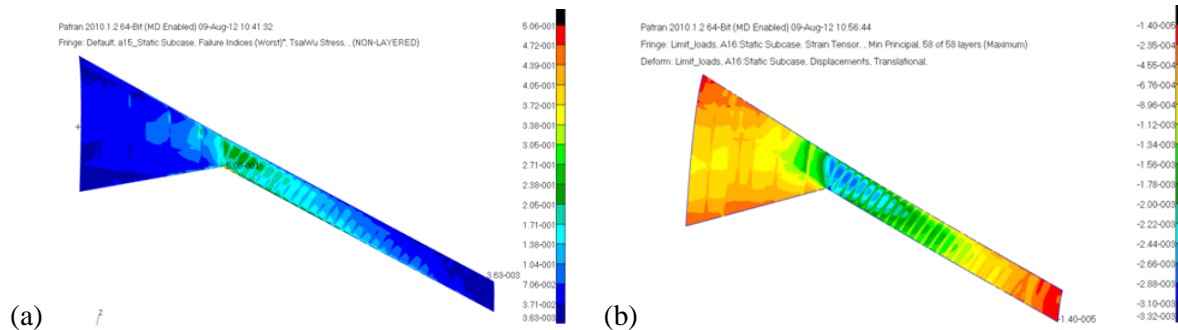
Figure 9. (a) FE results of FI and (b) strain plot of the upper wing skin under limit load

The structure was optimized with detailed FE analysis presented in Appendix E. As the final results under limit load, the maximum strains 3570 με and 3560 με occur in the lower skin and spars respectively (Appendix E, Fig.47). The results indicate that the preliminary design of the wing structure meets the strength requirements.

3.4   Structural FE modal and gust response analysis

Based on the FE model, modal analysis was carried out by using Nastran. The first a few frequencies in both empty fuel and full fuel cases are listed in Table 5, with the associated mode shapes in empty fuel case presented in Fig.10.

Table 5. The first a few frequencies in empty fuel and full fuel cases

	Empty mass	Full-fuel mass
1st bending mode (Hz)	1.40	0.69
2nd bending mode (Hz)	5.96	3.16
3rd bending mode (Hz)	11.73	6.80
1st torsion mode (Hz)	16.04	12.18

1st bending mode   2nd bending mode

12

3rd bending mode   1st torsion mode
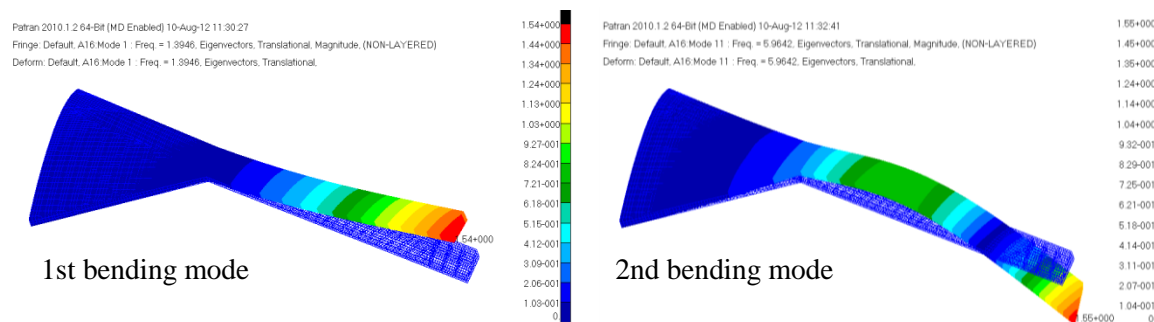
Figure 10. Normal modes of the wing in empty mass case

In the gust response analysis, three values of gust gradient were selected to consider the whole range from 9 m to 107 m. The three values and equiv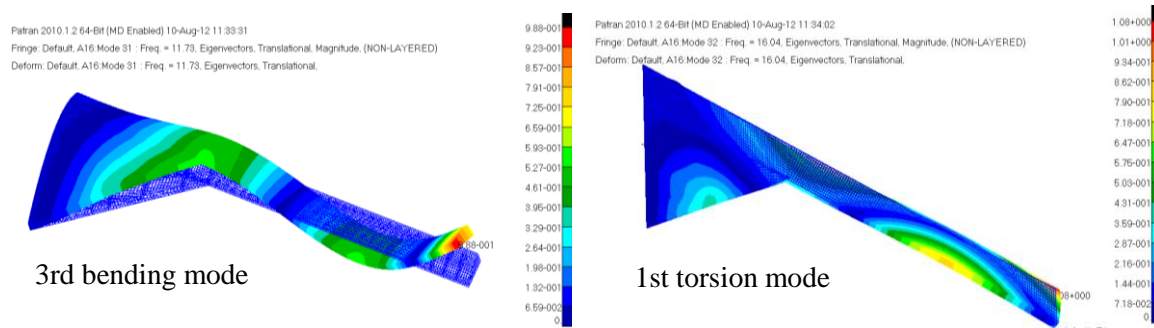alent gust frequencies are shown in Table 6. One of them is the typical gust gradient of 12.5 times the mean chord. It is noted that the gust load is in the range of the first three bending modes of the wing structure. This causes a concern of the wing structure, which is likely to be sensitive and have large response to gust load. The flight cases and data considered in the structural and gust load analysis are listed in Table 7.

Table 6. The gust gradient values and equivalent frequency

	H=9 m	H=12.5*chord=79.1 m	H=107 m
Frequency (Hz)	5.67	0.65	0.48

Table 7. Difference flight cases for gust response analysis

	Gust Case 1 Full Fuel	Gust Case 2 Empty	Cruise Case 1 Full Fuel	Cruise Case 2 Empty
Altitude (ft)	Sea level	Sea level	60000ft	60000ft
Weight (kg)	27674.22	11729.5	27674.22	11729.5
Mach No	0.3	0.3	0.65	0.65
Gust Load Factor	2.95	3.81	2.13	3.42

In the initial evaluation of the gust response based on the FE model, the gust load was calculated and applied as an external dynamic force on the aircraft clamped at the body center line in the same spanwise distribution as the aerodynamic force. Structural damping was considered,

but the rigid body motion is constrained. The aerodynamic damping and aeroelastic coupling was ignored. The most critical case at M=0.3 and sea level was considered in this case study.

In the empty fuel case, the gust response measured as displacement at wing tip is shown in Fig.11(a). From the results, it is noted that the maximum response was due to the gust of larger gust gradient *H*=79m and 107m corresponding to lower frequency range. Although the gust frequency is below the 1st bending mode, it is likely to excite the 1st mode and produce large response. It is also noted that the gust frequency of 5.67 Hz corresponding to the gust gradient *H*=9m is very close to the 2nd mode of 5.96 Hz and causes a long oscillation. However the deflection is much smaller than the larger gust gradient cases.

In the full fuel case, the gust response is shown in Fig.11(b). From the results, it is noted that the maximum response was corresponding to the gust gradient *H*=79m with the frequency 0.65 Hz very close to the wing 1st bending mode of 0.69Hz. This is the most critical case to be further investigated by considering the PGAD.

(a)   (b)

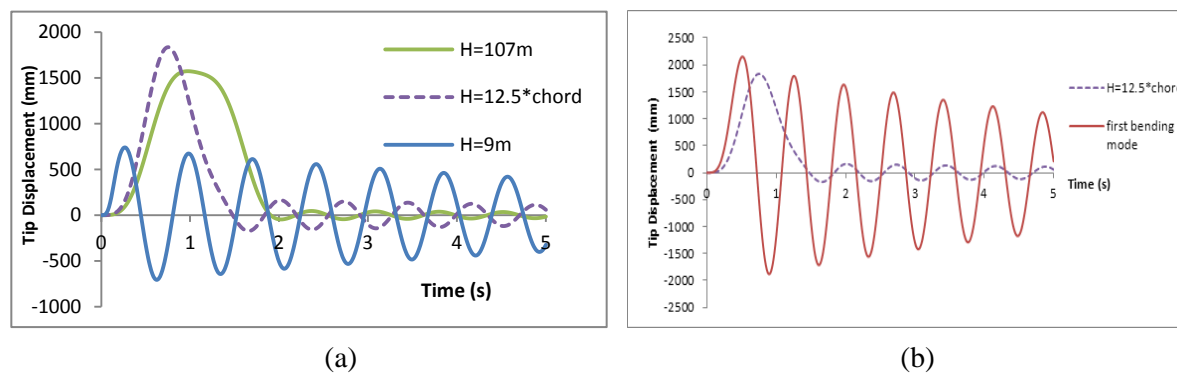**Figure 11. The gust response (a) in the empty fuel case and (b) in the full fuel case**

4. Gust Response Analysis of the Wing with PGAD

4.1 Beam model analysis

4.1.1. Wing beam model and gust response

The wing structure is then simplified by using beam model to consider the unsteady aerodynamics and aeroelastic coupling in the gust response analysis based on the theory presented

in section 2. The beam model is divided into 20 sections along the wing span plus one section representing the PGAD device of 1.85m in length connected to the beam model by a rotational spring. The nodes are located at shear center of wing sections assumed at 40% of the chord. The section bending and rotational stiffness are taken from cross sections of the section planes perpendicular to the neutral axis defined by 21 nodes. The mass distribution is transferred from the FE model. This makes sure that the same bending and rotational stiffness and similar mass distribution as the FE model are used for the beam model. Table 8 shows that the dynamic behavior of the simplified beam model in the full fuel case is very close to the FE model.

Table 8. The modal frequency from the wing FE and beam models

	FE Model	Beam Model
1st Bending Mode:	0.69 Hz	0.626 Hz
2nd Bending Mode:	3.16 Hz	3.104 Hz
3rd Bending Mode:	6.80 Hz	7.500 Hz
1st Torsion Mode:	12.18 Hz	13.22 Hz

In the following gust response analysis, only the most critical full fuel at sea level case was considered. Fig.12(a) shows the gust response of the wing to the three gust load frequencies listed in Table 6 without the PGAD. Fig.12(a) also shows the maximum response occurring in the typical gradient length at 0.65 Hz. Then the PGAD with three different design parameters was considered and results are shown in Fig.12(b) in comparison with the response without PGAD. In the figure, a=-0.3 and -0.9 represents the location of the rotation shaft is mounted at 30% and 90% of the semi-chord in front of the mid chord of the PGAD. The torque spring stiffness considered in the initial study is 40 kNm and 10 kNm.

Figure 12(b) shows that the gust response for the device shaft location a=-0.3 (located at 35% chord from leading edge) is greater than the case without the device. This is due to the shaft location being behind the pressure center of the surface and causing a positive rotation and lift. While the gust response for the device shaft location a=-0.9 (located 5% chord from leading edge) is significantly reduced especially for the 10kNm softer spring case. The results in Fig.12(b) shows that for the case of a= -0.9 and torque spring stiffness 40kNm, the gust response decrease

by 30% from 2.2m to 1.5m. This is due to a negative pitching moment generated by the device when the neutral axis is located ahead of the aerodynamic center.
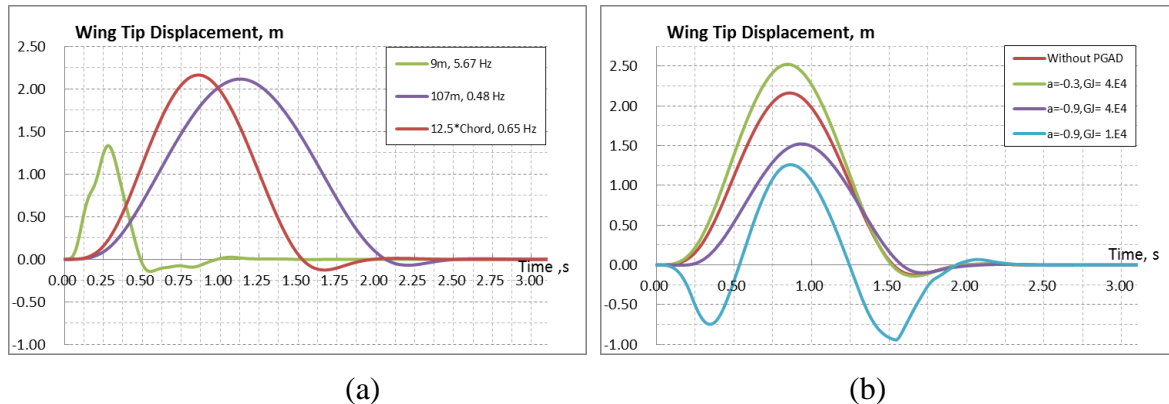

(a)   (b)

Figure 12.   The gust response of the wing (a) without PGAD and (b) with the PGAD

The device was set in a pitching degree of freedom from +10 degree to -20 degree at the connection section. In response to the gust, the wing deflects and rotates along the span and produce unsteady aerodynamic forces. Fig.13(a) shows the wing angle of attack (twist angle) associated with the gust response shown in Fig.12(b) at the section where the PGAD is mounted. Fig.13(b) shows the sum of the PGAD twist angle and the wing AoA at the wing tip. The gust generates a negative structure twist angle as a consequence of bending and torsion coupling of the large sweep back wing.
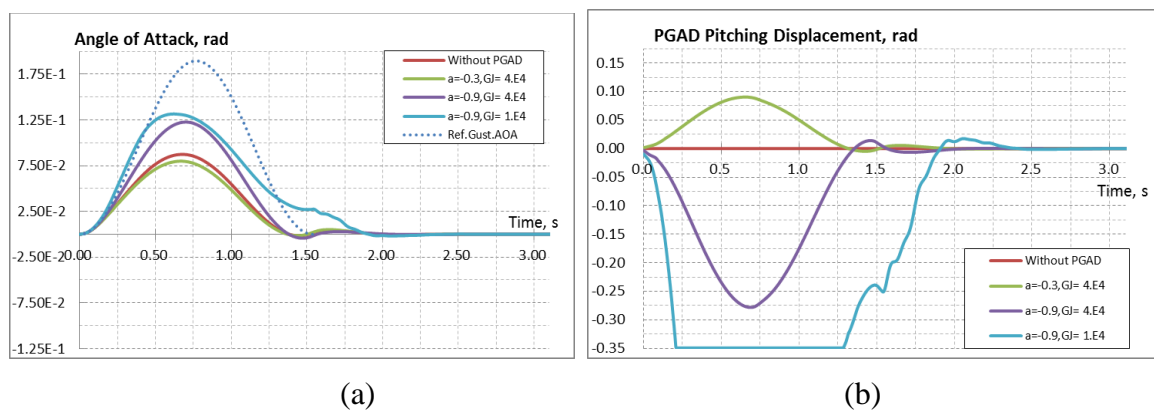

(a)   (b)

Figure 13. (a) AoA of the wing at wing tip (b) twist angle of the PGAD

16

For a low rotational stiffness spring, the gust generates a negative twist angle on the device and causes a sudden load reduction with a negative displacement at the early stage. With the increase of gust induced angle of attack, the lift and the response increase. The low spring stiffness allows the device twist reaches -20 degree limit as displayed in Fig.13(b).

By comparing the amplitude of different neutral axis location and spring rotational stiffness during the whole gust process, an optimal shaft location and spring stiffness can significantly reduce the gust response.

### 4.1.2. PGAD optimization for minimum gust response

The objective for optimization is to minimize the gust response by varying the shaft location and torque spring stiffness. A gradient based optimizer is applied in this optimization process.

$$\left\{ \begin{array}{c} MinW(x) \\ -0.1 \geq a \geq -0.9 \\ 80kNm \geq Ks \geq 10kNm \end{array} \right. \tag{11}$$

The torque spring stiffness is set as the design parameter at a given shaft location. The spring stiffness at three different shaft locations a= -0.1, -0.7 and -0.9 are optimized to achieve a minimum response. The shaft location at a= -0.5 which is the aerodynamics center location is taken as reference.

Fig.14(a) shows the optimal spring stiffness for the three shaft locations are 80kNm, 15kNm, and 31kNm with gust response of 2.41m, 1.11m, 1.2m respectively. Comparing with the reference response, the optimized stiffness leads to the gust response reduced by 48% and 45% for a=-0.7 and -0.9. The response decreases along with the shaft moving forward and spring stiffness decreasing.

A slightly smaller response occurs at a= -0.7 rather than a = -0.9. This is due to that a softer spring is quicker and easier to reach the lower bound of the twist angle limit for the device. However a sudden lift reduction could result in a higher response due to aeroelastic effect from the wing structure bending-torsion coupling.

(a)   (b)
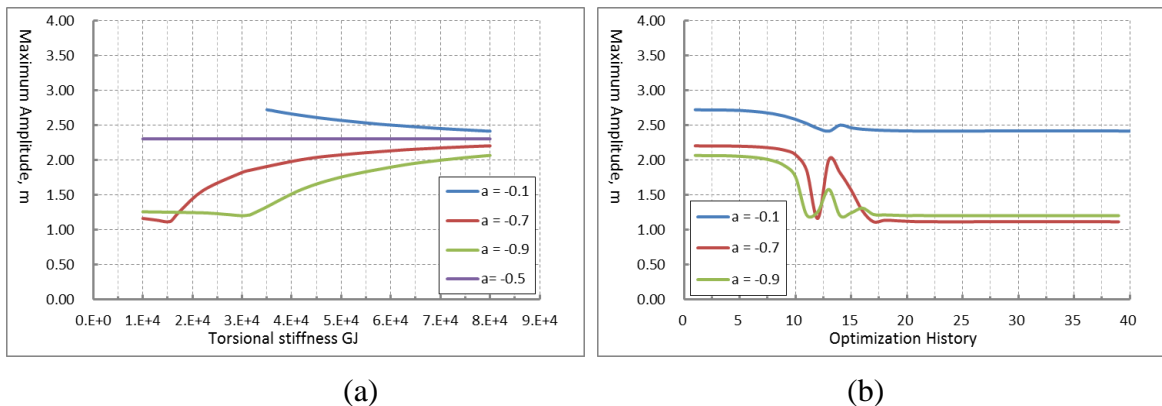
**Figure 14. (a) Optimized response varying with the spring stiffness
(b) Optimization history for different shaft locations**

In order to maintain the normal flight performance without gust, a practical design constraint is set to limit the PGAD twist angle to -2 degree during cruise. This will prevent a significant lift lost in normal flight. For the case of a=-0.7, the lower bound of the spring stiffness is 28kNm. Under this limit, the gust response is 1.79m with a gust load reduced by 17% comparing with the reference case.

4.2   3D FE model analysis

Based on the 3-D FE model of the whole aircraft (details in Appendix E), further gust analysis was carried out with the PGAD spanwise dimension increased from the previous 1.6 m to 2 m. However the torque spring stiffness was designed to limit the PGAD twist angle within 10 degree. To minimize the flow turbulence between wing and PGAD in action, the interface is set streamwise as shown in Fig.1a. Accordingly the shaft should be normal to the interface to make sure the PGAD can rotate freely. However, the PGAD could be designed with its elastic axis either in parallel to the shaft or to the front spar. Both cases were studied with the 1st case results presented in the following section and the second less effective case presented in Appendix F. The shaft location in chordwise (a) and spring stiffness (*GJ*) were taken as independent design variables. In the FE modeling, the shaft and torque spring are modeled by using spring elements.

18

The following gust alleviation analysis is presented in two parts. Firstly the rigid body motion of the aircraft was restricted by clamping the aircraft body center line as previous study. Then the aircraft is set free-free to take the rigid body motion effect into account.

4.2.1. Gust response for the shaft in parallel to global Y-axis

In the four different locations of the shaft a=-0.3, -0.5, -0.7 and -0.9 studied in previous beam model, only the practical and effective locations a=-0.3 and -0.7 with the typical gust gradient *H*=12.5 times chord was taken in the analysis.

In the case a=-0.7, the shaft is located exactly on the front spar (15% chord from leading edge), which is a practical position. A series of spring *GJ* values were studied and 3 typical results were presented in Table 9. Comparing with the previous results, much greater gust alleviation over 35% can be achieved when the PGAD twist angle was limited to -20 degree. Under the practical constraint for the PGAD twist angle -10° set as boundary, over 18% gust alleviation and 15% bending moment (wing root) reduction have been achieved. The torque spring stiffness was increased to 58 KNm/rad. Taken this spring stiffness, the gust response results in terms of PGAD twist angle, wing tip displacement and wing root bending moment for different shaft locations are shown in Fig. 15-17. Some of the results have been published in a conference [31].

Table 9. Gust response with PGAD shaft normal to streamline

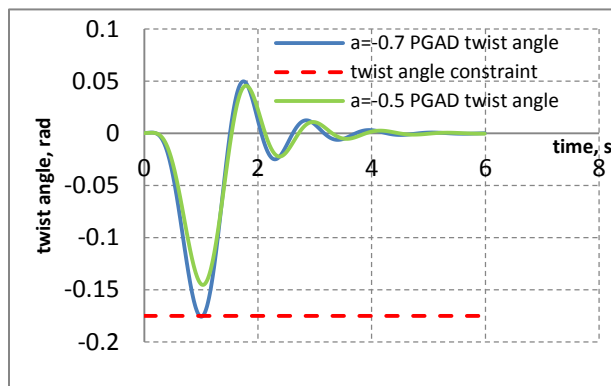| Case	Spring stiffness (Nm/rad)	Wing tip Disp. (m)	Disp. Reduction	Bending Moment (KNm)	BM Reduction	PGAD Relative Twist angle(°)
Initial design	/	3.07	/	5600	/	/
a=-0.7	2.8E4	1.99	35.2%	3987	28.8%	-19.7
	4.0E4	2.28	25.7%	4461	20.3%	-14.2
	5.8E4	2.51	18.2%	4760	15%	-10.0
a=-0.5	5.8E4	2.59	15.6%	5240	6.4%	-8.3

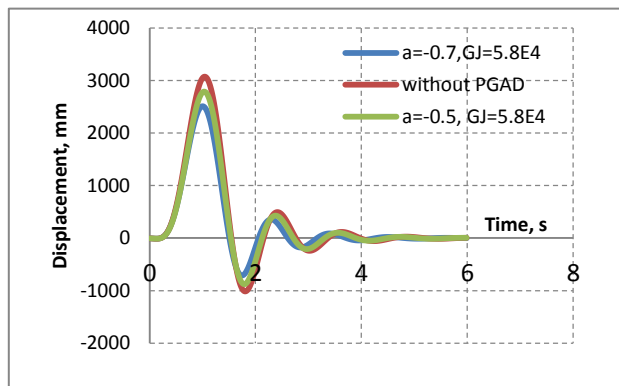Figure 15. PGAD twist angle in response to gust

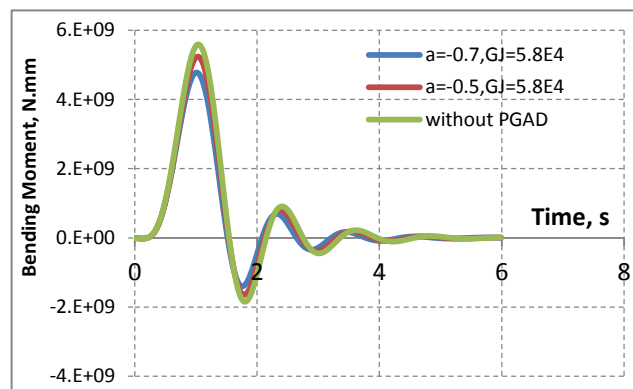Figure 16. Wing tip displacement response

Figure 17. Wing bending moment at root

All the above analysis produces relative values of the gust response to assess the effectiveness of the PGAD. Since the aircraft was clamped at its root, all the input energy from gust is assumed to be absorbed by the elastic structure. This results in an overestimation of the gust response and loading to the structure. In order to predict the real lift gust response, the constraint set to the aircraft should be removed to allow for a free-body motion as real life. The analysis and results are presented in the following section.

4.2.2. Gust response of the whole aircraft with free-body motion

In this free-body aircraft case study, only the degree of freedom in Z-direction was set free so that the wing can plunge freely in transverse direction. The reason for not being able to remove the pitching constraint was because the whole aircraft was not trimmed for stable level flight yet. The aircraft flight stability is beyond the current project scope. Nevertheless the transverse free

rigid-body motion makes the analysis condition much closer to real lift. In the analysis, only the most practical and effective shaft location a=-0.7 was taken as example. As shown in Figure 18, the PGAD twist angle is less than -10° (-0.175 rad) within the limit. The aircraft body (CG position) displacement and the wing elastic deformation measured at tip and the combined elastic and rigid body displacement at wing tip are presented in Fig.19. To compare with the previous results, the wing pure elastic gust response with and without PGAD is shown in Fig. 20. Figure 21 shows the resulting bending moment measured at wing root in response to the gust load. The results show that the gust induced maximum wing elastic deflection 0.65m without PGAD is reduced by 20% to about 0.52m and the bending moment is reduced by 17%.
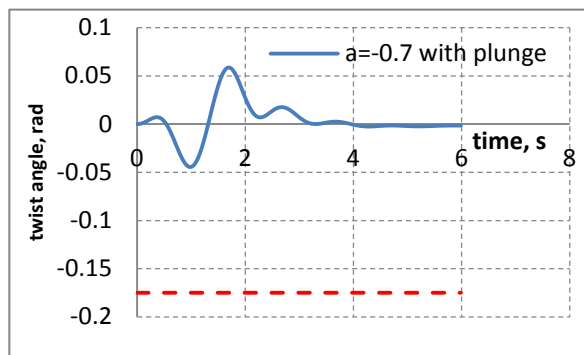

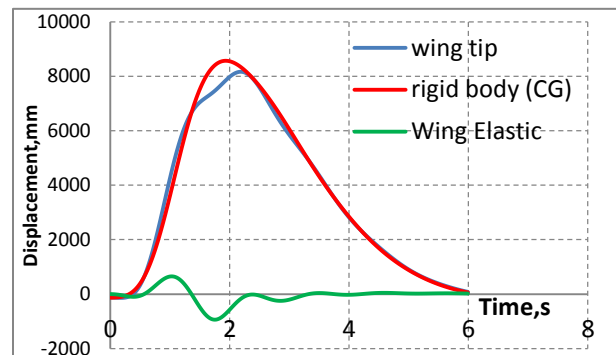**Figure 18. PGAD relative twist angle**
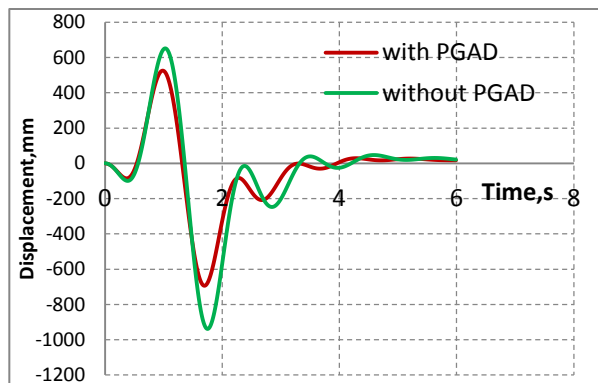

Figure 19. Wing tip displacement comparison
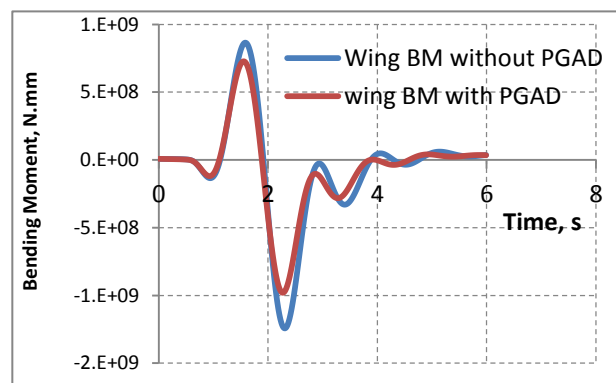

Figure 20. Wing tip elastic displacement

Figure 21 Wing bending moment response

21

5. Conclusions

The PGAD design concept was evaluated in this investigation. A full scale flying wing aircraft of high aspect ratio wing has been taken as an example to demonstrate the effectiveness of the PGAD for gust alleviation. Through the study, the following conclusions can be drawn.

- The aerodynamic analysis has been carried out by using high fidelity modeling methods. Detailed pressure distribution and flow features especially in the kink and wing tip regions have been predicted by using CFD method to produce accurate loading results.

- The mass distribution of the whole aircraft with the primary structure, systems, components and payload has been estimated for load prediction. However the mass distribution and CG location has not been tuned to meet level flight trim condition since the flight stability is beyond the project scope.

- Based on an initial design, detailed stress analysis of the whole aircraft structure modeled by FE method based on NASTRAN has been conducted to meet the design requirements. The maximum strain of the composite structure is limited to 3600 $\mu\varepsilon$ considering damage tolerance.

- Following the modal analysis of the structure, flutter speed of 241 m/s has been predicted using V-g method by NASTRAN.

- Since the fundamental frequency of this particular high aspect ratio flexible wing structure is only 0.69 Hz, the aircraft is very sensitive to the gust in the whole range of gust length. A significant gust response occurs in the specified flight condition at sea level. The investigation shows that a significant reduction of gust response can be achieved by using the PGAD. By optimizing the PGAD key parameters, a minimum gust response can be achieved.

- When the rigid-body motion of the aircraft is constrained, up to 35% gust alleviation can be achieved by using the optimized PGAD subject to -20° twist angle limit. When the twist angle is limited to -10°, the gust response in terms of wing tip deflection and wing root bending moment can be reduced by over 18% and 15% respectively.

- When the transverse rigid-body motion is set free under the 10° twist angle limit, the gust response in terms of wing elastic deflection and bending moment can be reduced by over 20% and 17% respectively.

References

[1] S Guo, W Cheung, JR. Banerjee and R Butlar, Gust alleviation and flutter suppression of an optimised composite wing, presented and published in Proc. of *the International Forum on Aeroelasticity and Structural Dynamics, Manchester*, U.K. June 1995, pp.41.1-41.9

[2] Britt, R., Jacobson, S., Arthurs, T, "Aeroservoelastic Analysis of the B-2 Bomber" *Journal of Aircraft* Vol 37, No. 5. September-October 2000

[3] GregoryW. Reich, Daniella E. Raveh, and P. Scott Zink, Application of Active-Aeroelastic-Wing Technology to a Joined-Wing Sensorcraft, *Journal of Aircraft* Vol. 41, No. 3, May–June 2004.

[4] Eric Vartio, Anthony Shimko, Carl P. Tilmann, Peter M. Flick, Structural Modal Control and Gust Load Alleviation for a SensorCraft Concept, the 46th AIAA/ASME/ASCE/AHS/ASC Structures, Structural Dynamics & Materials Conference, 18 - 21 April 2005, Austin, Texas AIAA 2005-1946

[5] Ronald W. Roberts, Robert A. Canfield, Maxwell Blair, Sensor-Craft Structural Optimization and Analytical Certification, *AIAA-2003-1458, 44th AIAA/ASME/ASCE /AHS Structures, Structural Dynamics, and Materials Conference*, Norfolk, Virginia, 7-10 April 2003

[6] C. P. Tilmann, P. M. Flick, C. A. Martin, M. H. Love, High-Altitude Long Endurance Technologies for SensorCraft, *RTO Paper MP-104-P-26, RTO AVT-099 Symposium on Novel and Emerging Vehicle and Vehicle Technology Concepts*, 7-11 April, 2003, Brussels, Belgium.

[7] Reich, G., Raveh, D., and Zink, P., Application of Active Aeroelastic Wing Technology to a Joined-Wing SensorCraft, *AIAA Paper 2002-1633, 43rd AIAA/ASME/ASCE/AHS/ASC Structures, Structural Dynamics, and Materials Conference*, April 2002.

[8] Reich, G. W., Bowman, J. C., and Sanders, B. Application of Adaptive Structures Technology to High Altitude Long Endurance Sensor Platforms*," Proc. 13th International Conference on Adaptive Structures and Technologies*, Germany, Oct. 7-9, 2002, pp. 423-434.

[9] Nangia, R.K., Palmer, M.E. & Tilmann, C.P., On Design of Unconventional High Aspect Ratio Joined-Wing Type Aircraft Configurations, *ICAS 2002*, Toronto.

[10] Joseph Henderson, Christofer Martin, Jayanth Kudva, "Sensitivity of Optimized Structures to Constraints and Performance Requirements for the SensorCraft ISR Platform", *44th AIAA/ASME/ASCE/AHS Structures, Structural Dynamics, and Materials Conference*, 7-10 April 2003, Norfolk, Virginia

[11] Donald H. Emero and Leonard Spunt, "Optimization of Multirib and Multiweb Wing Box Structures Under Shear and Moment Loads", *6th AIAA Structures and Materials Conference*, Palm Springs, California, April, 1965.

[12] ESDU No. 03001, "ELASTIC BUCKLING OF LONG, FLAT, SYMMETRICALLY-LAMINATED (ASBODF),COMPOSITE STIFFENED PANELS AND STRUTS IN COMPRESSION.", Engineering Science Data Unit International plc

[13] Niu, M.C. (1999), "Airframe Stress Analysis and Sizing (2nd edition)", Conmilit Press Ltd, Hong Kong.

[14] Armanios, E.A. and Badir, A.M. Free Vibration Analysis of Anisotropic Thin Walled Closed Cross-Section Beams, AIAA Journal, 1995, **33**, 1905–1910.

[15]Banerjee, J.R. and Williams, F.W. Free Vibration of Composite Beams – An Exact Method using Symbolic Computation, Journal of Aircraft, 1995, 32, 636–642.

[16]Wittrick, W.H. and Williams, F.W. A General Algorithm for Computing Natural Frequencies of Elastic Structures, Quarterly Journal of Mechanics & Applied Mathematics, 1971, 24, 263–284.

[17]Liani E., and Guo S. Potential-Flow-Based Aerodynamic analysis and test of a Flapping Wing, 37th AIAA Fluid dynamics Conference, AIAA-2007-4068, 2007.

[18]Theodorsen T. General Theory of Aerodynamic Instability and the Mechanism of Flutter, NACA Technical Report 496, 1949, 413- 433.

[19]S Guo, W Cheng, D Cui. Aeroelastic tailoring of composite wing structures by laminate lay-up optimization (TN), *AIAA Journal*, 2006, 44: 3146-3150

[20]Van Aken, J. M. (1986), An Investigation of Tip Planform Influence on the Aerodynamic Load Characteristics of a Semi-Span, Unswept Wing and Wing-Tip, NASA-CR-177428, NASA, Lawrence, Kansas.

[21]Anon (1977), "PROPERTIES OF A STANDARD ATMOSPHERE.", Engineering Sciences Data Unit, Data Items.

[22]Anderson, J. D. (2010), Fundamentals of Aerodynamics, Fifth edition, McGraw-Hill International Editions: Mechanical Engineering Series.

[23]Weissinger, J. and Naca (1947), The lift distribution of swept-back wings, Naca, Washington, D.C.

[24]Drela, M., Youngre, H. (2001), X-foil User manual, available at: http://web.mit.edu/aeroutil_v1.0/xfoil_doc.txt (accessed 07/06/2012).

[25]Symscape (2012), Why Use a Panel Method?, available at: http://www.symscape.com/blog/why_use_panel_method (accessed 25/05/2012).

[26]Graham, D. J., Nitzberg, G. E., Olsen, R. N. and Naca (1947), A systematic investigation of pressure distributions at high speeds over five representative NACA low-drag and conventional airfoil sections, Naca, Washington, D.C.

[27]ESDU International (1994), Shear force, bending moment and torque of rigid aircraft in symmetric steady manoeuvring flight.

[28]Hexcel Company (2012), Hexcel.com - Aerospace Products: HexTow, HexForce, Composites, available at: http://www.hexcel.com/products/aerospace/ (accessed 12/08/2012).

[29]College of Aeronautics (2002), CoALA, Laminate Analysis, Cranfield University.

[30]Howe, D. (2004), Aircraft Loading and Structural Layout, Professional Engineering Publishing.

[31]S Guo, Q.Fu, O.K. Sensburg, Optimal design of a passive gust alleviation device for a flying wing aircaft, 12th AIAA ATIO/14th AIAA/ISSMO MAO Conference, Session MAO-25, Indianapolis, Indiana, USA, 17-19 Sept. 2012

Appendix A. Aerodynamic Analysis

A.1 Initial analysis and Modified wing tip

A.1.1 Wing Geometry

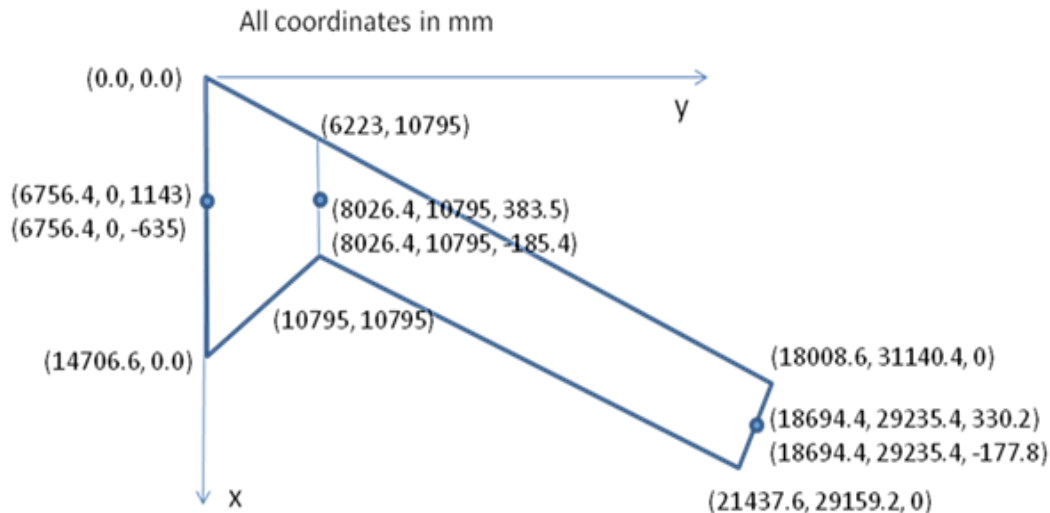The original geometry of the wing was presented in Fig.A1 as following:

Figure A1. Initial geometry of the wing

In order to carry the aerodynamic study, an aerofoil had to be chosen to fit as close as possible to coordinates given in the specifications. The only data given on the aerofoil shape was the thickness of 15% of the chord. A research of the available aerofoils for the specified thickness was conducted. From the sixteen aerofoils selected, none was fitting perfectly with the coordinates of the geometry. However, with the approval of Dr Guo, the standard aerofoil NACA 4415 as shown in Fig. A.2 was chosen, as it has one of the highest lift coefficients for AoA=0° (~0.50 for Reynolds Numbers of 106). Indeed, zero angle of attack was the reference angle of attack to begin the aerodynamic analysis.
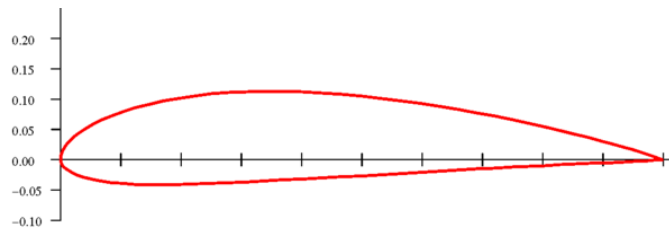
Figure A2. NACA 4415 aerofoil

A.1.2 Flight Cases

Two different cases were used within the aerodynamic analyses and then compared [21]:

- Critical Gust Case at Full-Fuel Weight, Sea level, Mach 0.30:

  - Air density ρ= 1.225 kg/m3
  - Kinematic density ν=1.46x10-5 m²/s
  - Velocity v=102 m/s
  - Mass: 27674.22 kg (semi span)

- Cruise Case at Full-Fuel Weight, 60000 ft, Mach 0.65:

  - Air density ρ= 0.115 kg/m3
  - Kinematic density ν=1.23x10-4 m²/s
  - Velocity v=191.8 m/s
  - Mass: 27674.22 kg (semi span)

The aerodynamic analyses of these study cases were first performed with zero angle of attack.

A.2.1 Initial CFD analysis

Initial calculations of the lift distribution of this geometry were conducted by using the CFD software FLUENT. From the first results of the analysis, it appeared a sudden drop of the lift at the tip of the wing. As shown in the Fig. A3, the lift decreases significantly and becomes negative from 30m spanwise to the wing tip. This phenomenon can be explained by the turbulences created by the angled wing tip. Indeed, the wing tip shape has a large influence on the aerodynamic characteristics at the tip. Investigations have been conducted on the influence of the tip characteristics on the wing aerodynamic characteristics [20]. This study has shown by wind tunnel

27

experiments that the non-alignment of the tip boundary with the streamlined flow increases local drag and lowers the local lift.
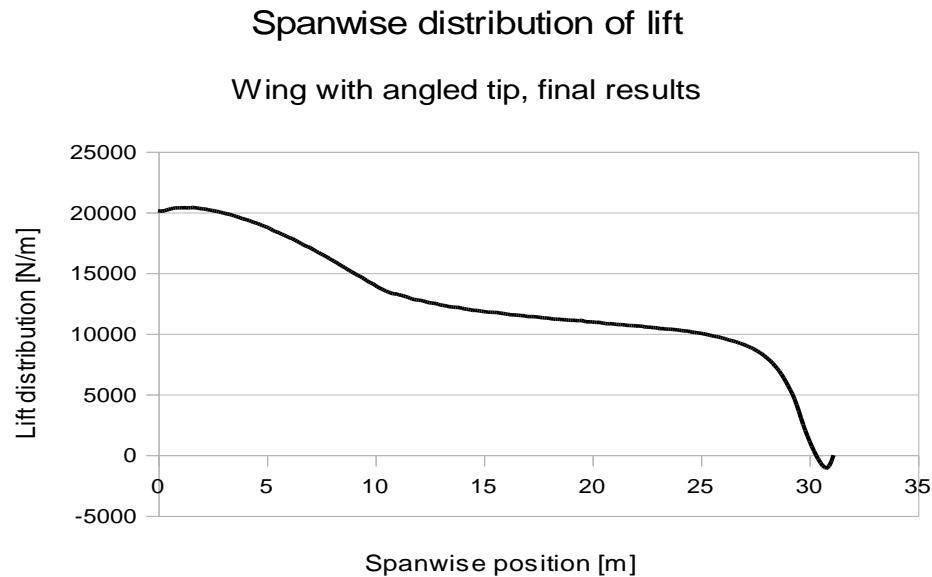
Spanwise distribution of lift

Wing with angled tip, final results

Figure A3. Lift distribution for the geometry with angled tip (AoA=0°, M=0.30)

A.2.2 Modified wing tip geometry

The original angled wing tip geometry will affect the accuracy of CFD simulation. The loss of pressure would also have negative effect on the PGAD effectiveness. Therefore, a modified geometry was proposed to minimize the impact. The original wing was extended and then cut at y=31.14 m in parallel to xz plane to make the tip section aligned with the upstream flow velocity as shown in Fig. A.4
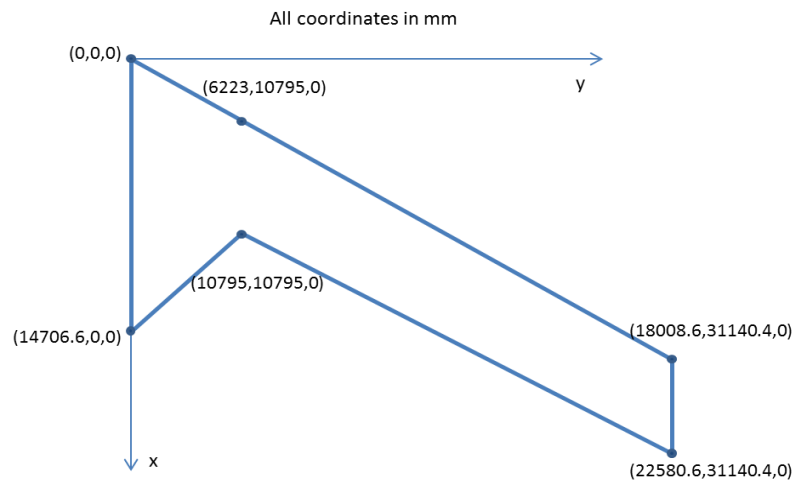
All coordinates in mm

(0,0,0)

(6223,10795,0)

y

(10795,10795,0)

(14706.6,0,0)

(18008.6,31140.4,0)

x

(22580.6,31140.4,0)

Figure A4. Final wing geometry

With this new configuration, the CFD analysis showed that the drop of the lift at the tip was eliminated. With this tip configuration, the lift distribution has a smoother shape at the tip and keeps a positive value at the tip.

A.2 Aerodynamic methods

A.2.1 The Lanchester-Prandtl Theory

The lift distribution of a three-dimensional wing is not the successive analyses of the two-dimensional cross-sections along the span. Indeed, the lift created on each wing section depends on the characteristics of the section but also on the lift created by the neighbouring sections. The Lanchester-Prandtl Theory, named also as the Prandtl's Lifting Line Theory is a theoretical model of the lift distribution based on the three-dimensional wing geometry [22]. This theory was elaborated at the beginning of the 20th century and is still used for preliminary calculations.

The main assumptions of this theory are:

- The flow is a steady potential flow: inviscid and irrotational
- The flow is incompressible
- High aspect ratio wing

29

-    Low sweep angle

The three-dimensional wing is discretised into multiple spanwise sections. Each section is modelled by a horseshoe vortex, which is the combination of a bound vortex and two free-trailing vortices which extend downstream. Multiple bound vortices are all aligned along a single line, the lifting line represented in the Figure A5, conventionally located at the quarter chord line.
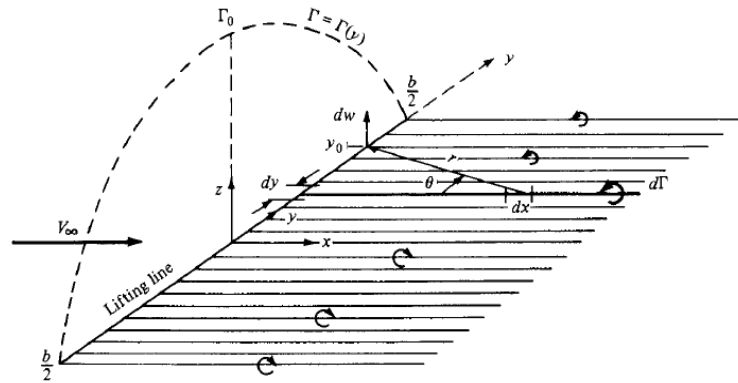

Figure A2. Horseshoe vortices and the Lifting Line [22]

The theory relates the circulation Γ and the lift per unit span using the Kutta–Joukowski theorem:

$$L' = \rho_\infty V_\infty \Gamma \qquad \text{(A.1)}$$

Where:

-    L' is the lift per unit span

-    ρ_∞ is the freestream density of the fluid

-    V_∞ is the freestream velocity of the fluid

The downwash induced by the trailing edge vortices is calculated for each horseshoe vortex. The downwash at the point y_0 is induced by all the trailing vortices along the lifting line. The trailing vortex at the coordinate y creates a downwash dw at the point y_0 given by the Biot-Savart law:

$$dw = -\frac{(d\Gamma/dy)dy}{4\pi(y_0 - y)} \qquad \text{(A.2)}$$

The total downwash at the point y_0 is the sum of the effects of all the trailing vortices along the lifting line:

$$w(y_0) = -\frac{1}{4\pi} \int_{-b/2}^{b/2} \frac{(d\Gamma/dy)dy}{y_0 - y} \tag{A.3}$$

The downwash affects the local flow along the span. The effective angle of attack α_{eff} depends on the geometrical angle of attack α of the section but also on the induced angle of attack due to the downwash α_i:

$$\alpha_{eff}(y_0) = \alpha(y_0) - \alpha_i(y_0) \tag{A.4}$$

Where:

$$\alpha_i(y_0) = \frac{1}{4\pi V_\infty} \int_{-b/2}^{b/2} \frac{(d\Gamma/dy)dy}{y_0 - y} \tag{A.5}$$

And

$$\alpha_{eff}(y_0) = \frac{\Gamma(y_0)}{\pi V_\infty c(y_0)} + \alpha_{L=0} \tag{A.6}$$

$\alpha_{L=0}$ is the zero-lift angle of attack, known from the aerofoil characteristics
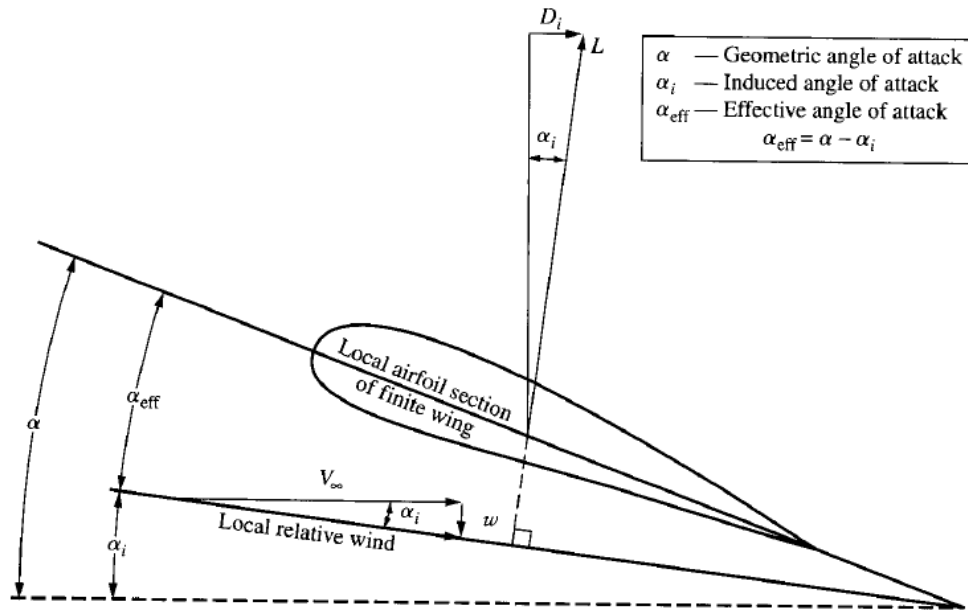

Figure 3: Effect of the downwash on the angle of attack [22]

The unique unknown of these equations is the circulation Γ. To calculate it, the following transformations are done:

$$y = -\frac{b}{2}\cos\theta \tag{A.7}$$

And

$$\Gamma(\theta) = \Gamma_0 \sin\theta \tag{A.8}$$

31

With $0 \leq \theta \leq \pi$

The Fourier series are used to approximate the expression of the circulation. The accuracy of the approximation depends on the number of terms used. The more terms are used, the more accurate is the approximation, but the more complex will be the resolution of the system.

So,

$$\Gamma(\theta_0) = 2bV_\infty \sum_1^N A_n \sin n\theta_0 \qquad \text{(A.9)}$$

Hence, the equation (A.4) becomes:

$$\alpha(\theta_0) = \frac{2b}{\pi c(\theta_0)} \sum_1^N A_n \sin n\theta_0 + \alpha_{L=0}(\theta_0) + \sum_1^N n A_n \frac{\sin n\theta_0}{\sin \theta_0} \qquad \text{(A.10)}$$

For a given θ_0, which corresponds to a spanwise location, the previous equation is evaluated. Hence, as there are N A_n unknowns, the procedure is repeated for N different spanwise locations to be able to solve the system.

From these equations, the drag, the local lift coefficient can also be calculated.

In order to compare the different methods of calculation of the lift distribution, an equivalent model of the wing studied was created. A straight rectangular wing of a semi-span of 31.14 m, chord of 4.57 m, using NACA 4415 was analysed. This wing model is based on the wing geometry in the specifications. The outer part of the wing, from the kink at 10.5 m to the tip is taken as a model. The swept back angle is neglected in this application and the same geometry as from the outer part is used for the inner wing geometry from the root to the kink.
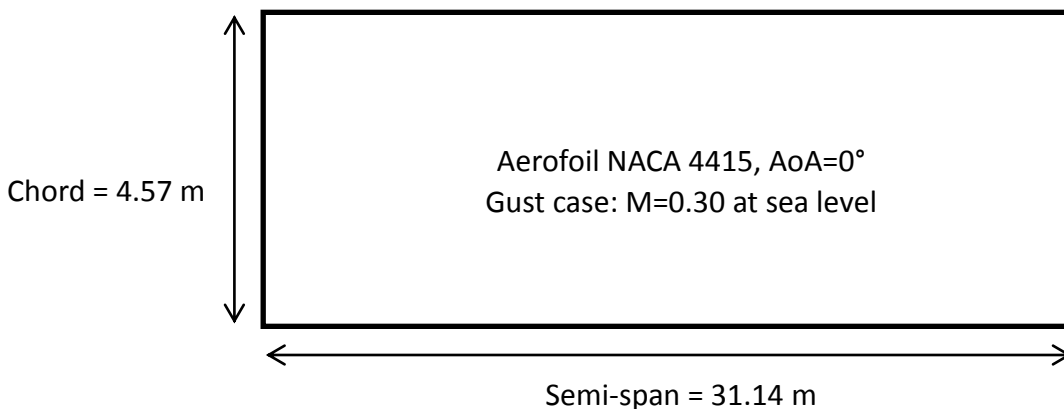

Figure A4: Rectangular wing geometry

The lift distribution was computed writing the previous equations in Matlab and solving the system. The result is obtained by dividing the wing span in 20 sections. The calculated lift distribution is presented in the Figure A8.
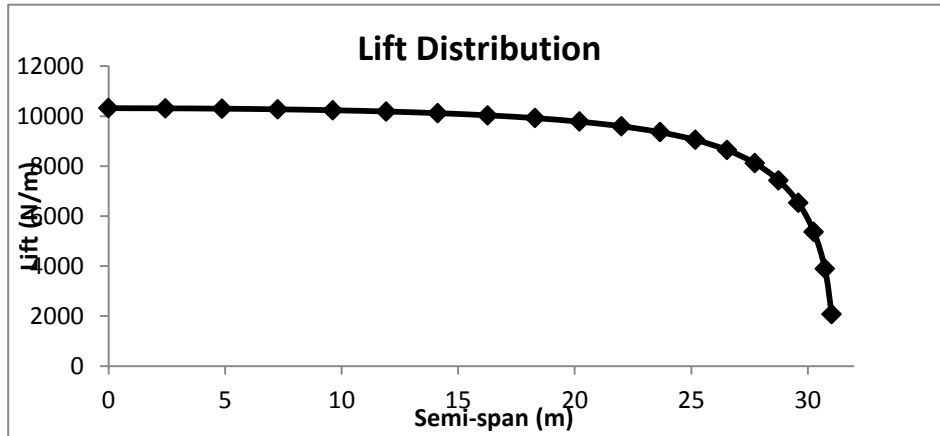

Figure A5: Lift Distribution of the rectangular wing model (M=0.3, AoA=0°)

The lift distribution obtained with this theory has an elliptical shape. This lift distribution is compared with the other methods further in the chapter where the effects of the different assumptions are discussed.

A.2.2 The Weissinger Theory

The Weissinger Theory [23] is based on the Lifting Line Theory but accommodates it to swept-back wings. Coefficients taking into account the swept back angle are added to the circulation equations presented in the Lanchester-Prandtl Theory. The total circulation is the circulation from the Lifting Line Theory plus a correction term which takes into account the sweep of the wing. The 'Influence function' L is used for the correction term:

$$L[\lambda(\overline{y_0} - \bar{y})] = \frac{\sqrt{1 + \lambda^2(\overline{y_0} - \bar{y})^2} - 1}{\lambda(\overline{y_0} - \bar{y})} \quad \text{(A.11)}$$

Where :

- $\lambda(y) = \frac{b}{c(y)}$ is the local aspect ratio

- $\overline{y_0} = \frac{y_0}{b/2}$ dimensionless coordinate in the absolute plane

33

- $\bar{y} = \frac{y}{b/2}$ dimensionless coordinate in the vortex plane

So the equation (A.3) becomes:

$$w(\overline{y_0}) = -\frac{1}{2\pi b}\int_{-1}^{1}\frac{d\Gamma/d\bar{y}}{\overline{y_0}-\bar{y}}\big[2+\lambda(\overline{y_0}-\bar{y})L[\lambda(\overline{y_0}-\bar{y})]\big]d\bar{y} \qquad (3.12)$$

However, this theory is more complex to apply than the Lifting Line Theory and would be time-consuming. Thus, the author preferred to use directly computational methods to determine and compare the lift distribution to the basic theory of Prandtl.

A.2.3 Computational Analyses: XFLR5

The aerodynamic studies were performed using two different softwares, FLUENT CFD and XFLR5. In parallel, the author computed the same cases in XFLR5.

The first step in the XFLR5 software is to set up the aerofoil of the wing. This analysis in 2D is performed using the software X-foil, included in the XFLR5 package.

The aerofoil NACA 4415 was studied for different conditions, i.e. various Reynolds numbers and angles of attack. The Reynolds number depends on the study case and the wing chord.

$$Re = \frac{VL}{v} \qquad (A.13)$$

Where L is a characteristic linear dimension, here the local chord.

The range of the Reynolds number for the geometry is very large. The minimum Reynolds number is located from the kink at 10.5 m spanwise to the wing tip, where the chord is the smallest and reaches the value of 7.106 for the cruise case. The maximum value of the Reynolds number is 1.108 at the root chord for the gust case. For all cases, the Reynolds number is high along the geometry. The viscosity is a characteristic of the fluid to consider for this study and in particular for high angles of attack where flow separation occurs. The X-foil analysis of the lift coefficient for the NACA 4415 has been conducted at different Reynolds numbers. The Reynolds number used by X-foil takes the characteristic dimension, the chord, as one. Thus, the range of Reynolds numbers to be calculated by X-foil at the different cases is between 1.6.106 and 7.106 [24].
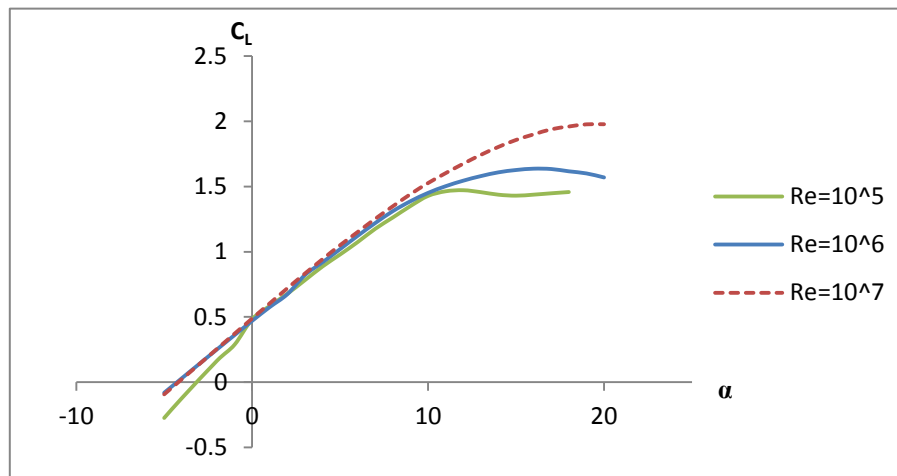
Figure A6: Lift coefficient vs. α (at different Reynolds numbers, by unit chord)

The software XFLR5 computes aerodynamic data in three dimensions. Once the aerofoil was defined in the software, the wing geometry was created following the coordinates given in the previous paragraphs for the new geometry. Several analyses were conducted to determine the spanwise lift distribution and pitching moment. The local lift coefficient C_L and the local pitching moment coefficient C_m were obtained using both the Vortex Lattice Method (VLM) and the 3D Panels Method. The Vortex Lattice Method and 3D Panels Method are two methods available in the software to compute the aerodynamic loads.
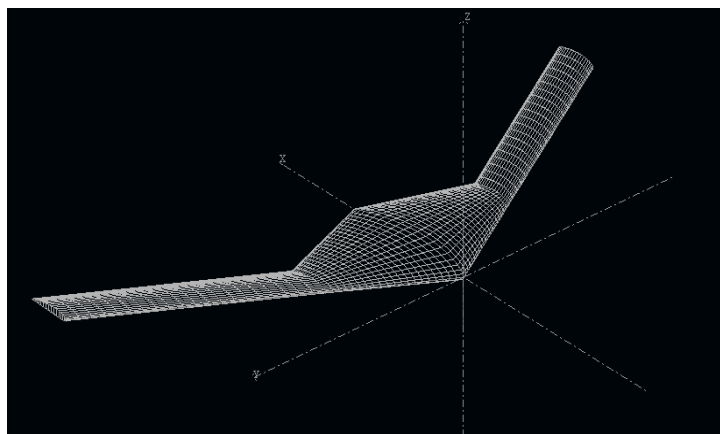

Figure A7: Wing geometry in XFLR 5

The VLM simplifies the wing geometry in an equivalent 2D geometry divided into panels. A discrete horseshoe vortex is applied at the control point of each panel. The theory of the VLM is based on the Laplace's equations and is an extension of the Lifting Line Theory. For each panel, the velocities and singularities induced by the vortex are computed. Thus, the pressure on the surfaces, the lift and the drag are calculated.

However this method does not take into account the viscosity and compressibility of the airflows. These assumptions reduce the range of the applications, since only subsonic flow can be modelled (Mach number<1). Although the VLM relies on the theory of ideal flow and thus the Laplace's equations, the compressibility of the flows can be corrected for high subsonic speeds by using the Prandtl–Glauert transformation:

$$c_p = \frac{c_{p0}}{\sqrt{1 - M^2}}$$
(A.14)

The formula can be used for the lift, drag and pitching moment coefficients as they are linear integrals of the pressure coefficient.

On the other hand, since the viscosity of the fluid is not considered in the calculations, the skin-friction drag is not added to the total drag. The influence of the thickness is not taken into account in the calculations using VLM as well. However, the 3D Panels Method models the wing in three dimensions, discretizing the span into panels following the aerofoil curve. The curves are idealized by straight lines at each aerofoil section. Therefore, both upper and lower surface characteristics are considered separately in the calculations. Although the 3D Panels Method has the same theoretical restrictions as the Vortex Lattice Method, this method has the advantage of considering the thickness of the aerofoil.

For low Mach numbers (M<0.3) and high Reynolds numbers (Re>105), these assumptions can be done to obtain initial results using these relative easy and rapid methods [25]. The lift distribution, pitching moment distribution and location of the centre of pressure along the span were extracted from the two methods. The results are compared to the other methods, and particularly to the CFD results in the next paragraph. However, additional calculations were needed after the acquisition of the data from the software in order to obtain the desired

36

information. For example, the location of the aerodynamic centre along the span, which is important for the load calculation (cf. Appendix B), was calculated from the results of the centre of pressure.
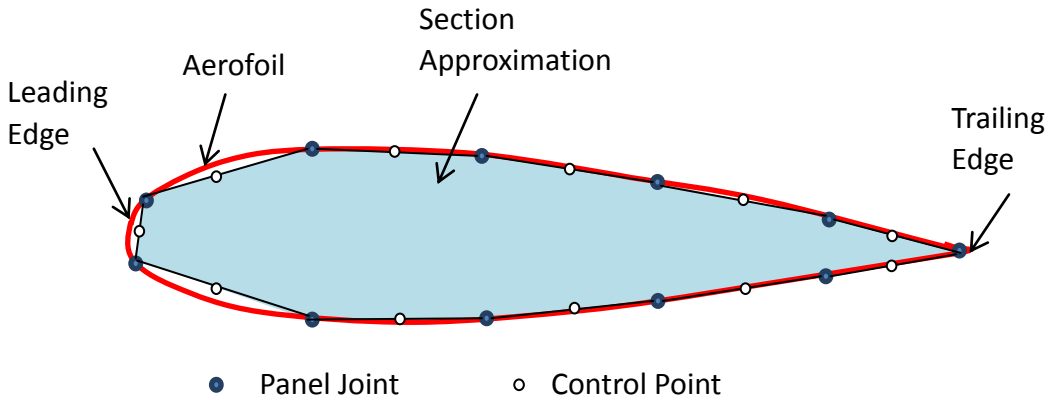

Figure A8: 3D Panels approximation to an aerofoil

From the two methods used in XFLR5, the centre of pressure was located along the span. The centre of pressure is the point where the total lift of the section applies without creating any moment.

Although the aerodynamic centre is often assumed at one quarter of the chord, the aerodynamic centre location for this geometry was computed from the centre of pressure location for different angles of attack in order to verify this common assumption.

The aerodynamic centre is the point where the pitching moment coefficient of the section does not vary with the lift coefficient:

$$\frac{dC_m}{dC_L} = 0 \qquad \text{(A.15)}$$

Since the lift coefficient at a given station depends only on the angle of attack at given flow conditions, and:

$$L' = \frac{1}{2}\rho c C_L V^2 \qquad \text{(A.16)}$$

$$M' = \frac{1}{2}\rho c^2 C_m V^2 \qquad \text{(A.17)}$$
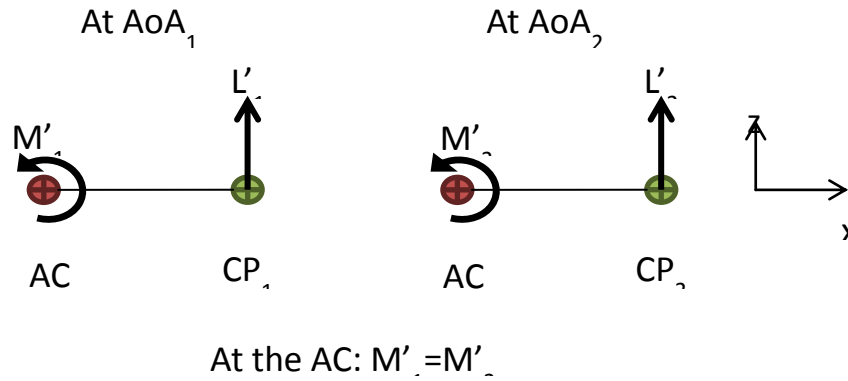
37

At the AC: M'₁=M'₂

Figure A9: Moment at the aerodynamic centre

As presented in the Figure A12, the aerodynamic centre location can be calculated as following:

$$L'_1(x_{CP1} - x_{AC}) = L'_2(x_{CP2} - x_{AC})$$ (A.18)

So,

$$x_{AC} = \frac{L'_2 x_{CP2} - L'_1 x_{CP1}}{L'_2 - L'_1}$$ (A.19)

Once the results were obtained with XFLR5, the lift distribution, pitching moment distribution, aerodynamic centre location were then compared to the CFD analyses results.

A.3 Comparison to the CFD Analysis

The VLM, Lifting line and 3D Panels method results can be compared to available in house Computational Fluid Dynamics (CFD) results which used the same geometry. The commercial software Fluent was used. The calculations with CFD take into account the viscosity and compressibility. The mesh can be denser at critical points in the flow field to capture the flow physics better. This is especially important for regions with high gradients.

The results of the different analysis methods described previously were compared for the two study cases. The initial data gave an angle of attack of 0° for both cases.

A.3.1 Gust Case: Sea Level, Mach 0.3

The Figure A13 presents the results obtained for the spanwise lift distribution using different methods for the gust case with an angle of attack of 0°. The VLM and 3D Panels method give

values very close to the CFD calculations with a maximum difference of 10%. The shape of the distributions is quite the same except at the tip of the wing where we can observe a drop of the lift at 31 m of the span in the CFD analysis whereas the VLM, 3D Panels lift distributions keep a smooth decreasing curve.
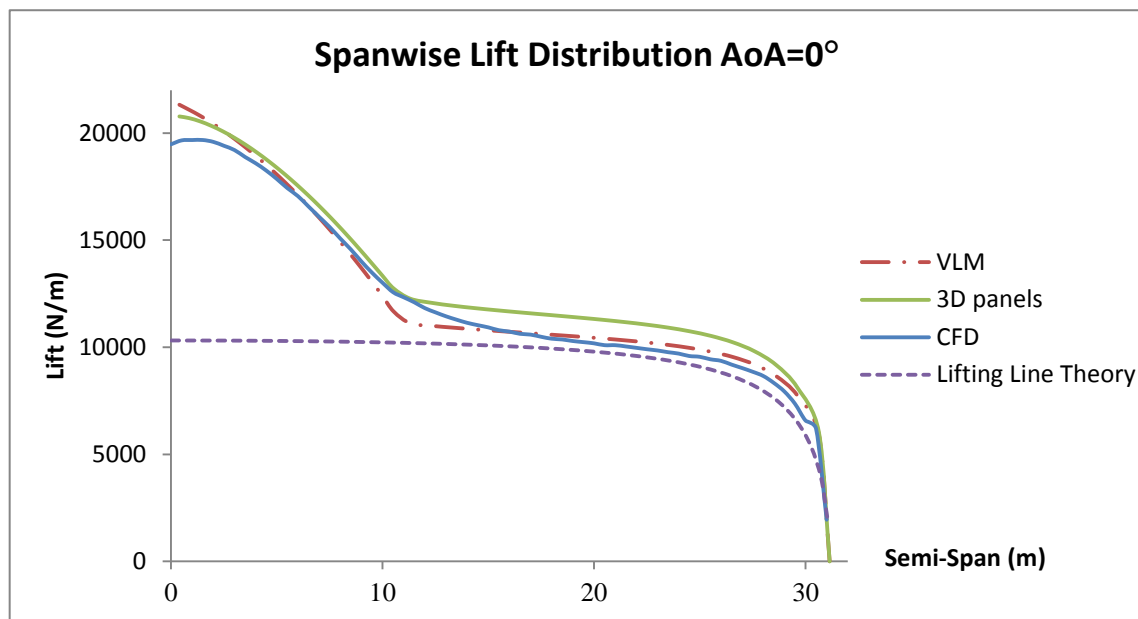

Figure A10: Spanwise lift distribution for gust case (AoA=0°)

   The Lifting Line Theory gives values close to the other methods for the straight swept part from 10.5 m to the tip even if this method tends to simplify the lift distribution by doing many assumptions. However, the difference in the accuracy of the method compared to the others is highlighted by under evaluating the lift, reaching a difference of 20% at the kink (10.5 m spanwise). The results from the root to the kink are not relevant with this method and cannot compared to the other method's results as the idealized geometry presented in the paragraph A.2.1 represents only the part of the geometry from the kink to the tip of the wing.

As the total lift created by the wing was higher than the weight that balanced the aircraft, the angle of attack of the aerofoil was reduced to -1°. With this new configuration, the equilibrium is maintained.
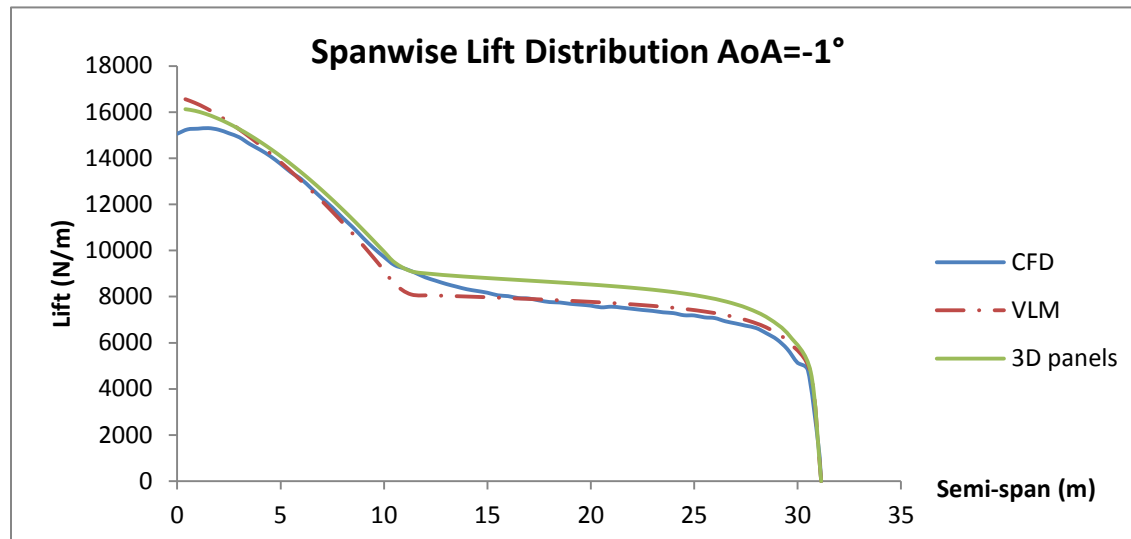
Figure A11: Spanwise lift distribution for gust case (AoA=-1°)

The new lift distributions have the same shape as the previous one for zero angle of attack. The total lift has been reduced from 380 kN to 300 kN.

Figure A12: Location of the aerodynamic centre for gust case

It can be highlighted in the Figure 15 that all the methods mostly calculate the aerodynamic centre located between 24% and 28% of the chord along the span except at the tip where the tip vortex affects the lift distribution. The 3D Panels method diverges from the other results at the root but

follows the same trend as the CFD at the wing tip. From the CFD results, it can be showed that the aerodynamic centre moves backward at the tip, located at 39% of the chord. This phenomenon has alr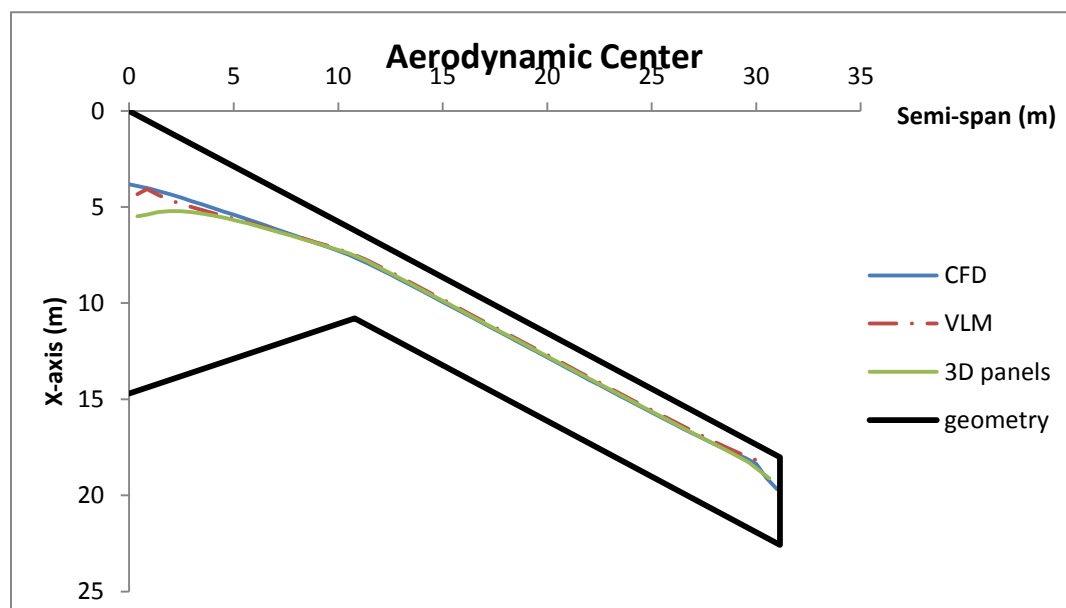eady noticed in previous experiments [20]. Nevertheless, the common assumption which gives the location of the aerodynamic centre at the quarter chord can be validated for most of the span. Therefore, the exact values of the aerodynamic centre were taken from the CFD for the following studies, as the CFD is considered as the most accurate method.
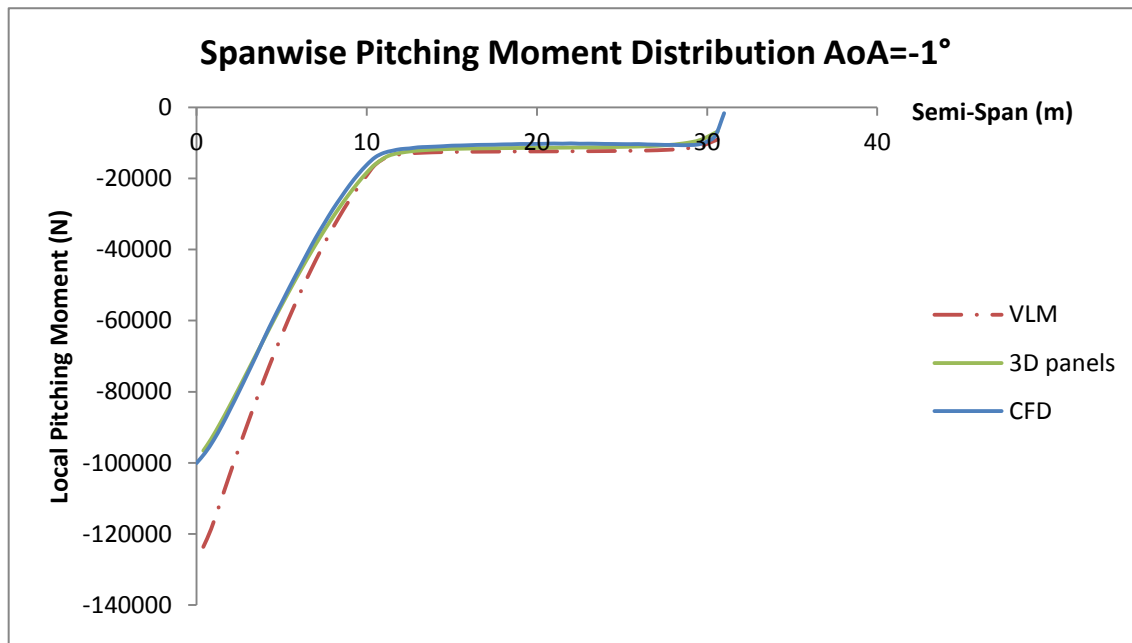
Figure A13: Spanwise pitching moment distribution for gust case (AoA=-1°)

The three methods CFD, VLM and 3D panels give the same results of pitching moment from 10.5 m to the tip of the wing which corresponds to the straight swept part of the wing. The pitching moment decreases rapidly to the root of the wing. However, the VLM results diverge from the other results for the triangular part of the wing.

A.3.2 Cruise Case: 60000 ft, Mach 0.65

As done for the gust case, the lift distribution was computed for the cruise case (altitude 60000 ft and M=0.65). The CFD, VLM, 3D Panels and Lifting Line methods results are compared in the Figure 17 for the angle of attack 0° as given in the specifications.

41

Figure A14: Spanwise lift distribution for cruise case (AoA=0°)

The results from the different methods are close and follow the same trends. As explained for the gust case, only the results from 10.5 m spanwise are relevant for the lifting line theory. The discrepancy bet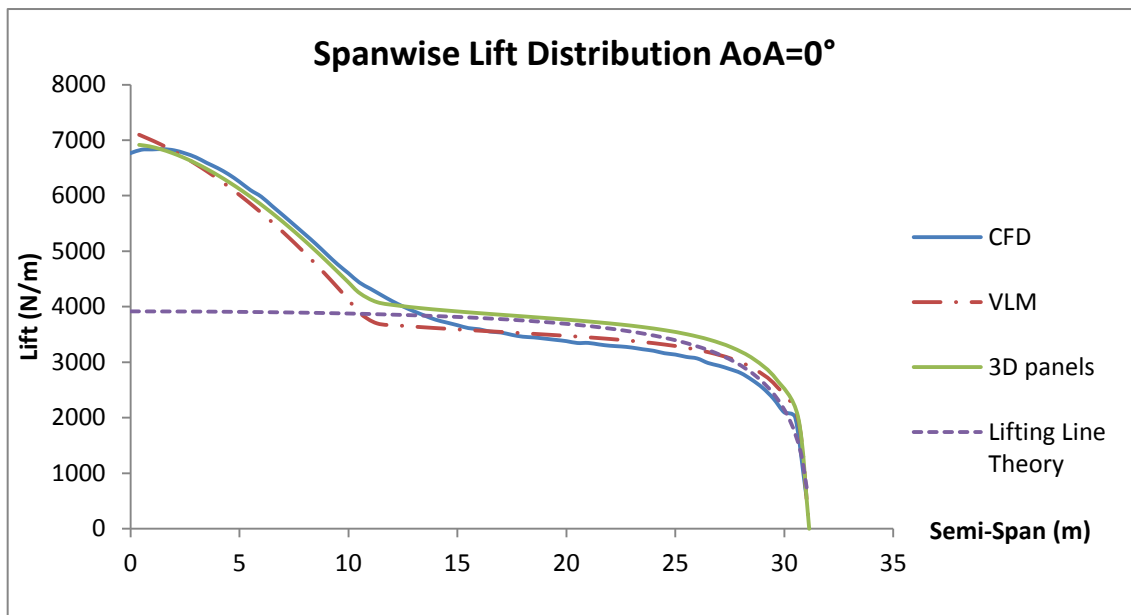ween the wing tip lift calculated using XFLR5 and CFD increases compared to the gust case. The discrepancy reaches 14% between the 3D Panels results and the CFD results at 28.5 m spanwise.

However, the analyses revealed that the total lift created by the wing in these conditions do not reach a sufficient value to counterbalance the weight of the aircraft. In these conditions, the lift decreases by more than half compared to the gust case. The total lift is 131 kN which is not enough for the maximum weight of 271 kN, even if it is assumed that 20 % of the fuel has been burned to reach this altitude.

In order to achieve the lift needed for the cruise, analyses have been computed for the same freestream conditions but increasing the angle of attack. As presented in the Figure A9, the lift coefficient C_L increases when the angle of attack increases between zero and ten degrees. The analyses have shown that an angle of attack of 5° is required to have enough lift for the case.

42
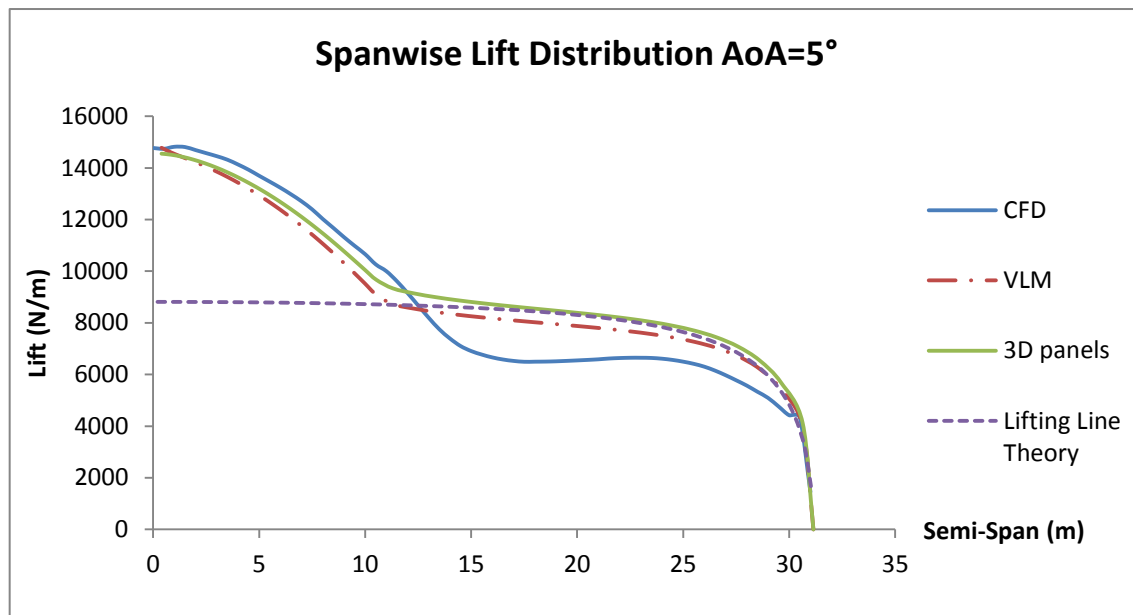
Figure A15: Spanwise lift distribution for cruise case (AoA=5°)

It can be noticed in the Figure 30 that the lift distribution calculated from XFLR5's methods and the Lifting Line Theory diverge from the CFD results. This is especially visible for the straight swept part from 10.5 m to the tip. The lower lift from the CFD can be attributed to a local flow separation at the kink in the geometry.
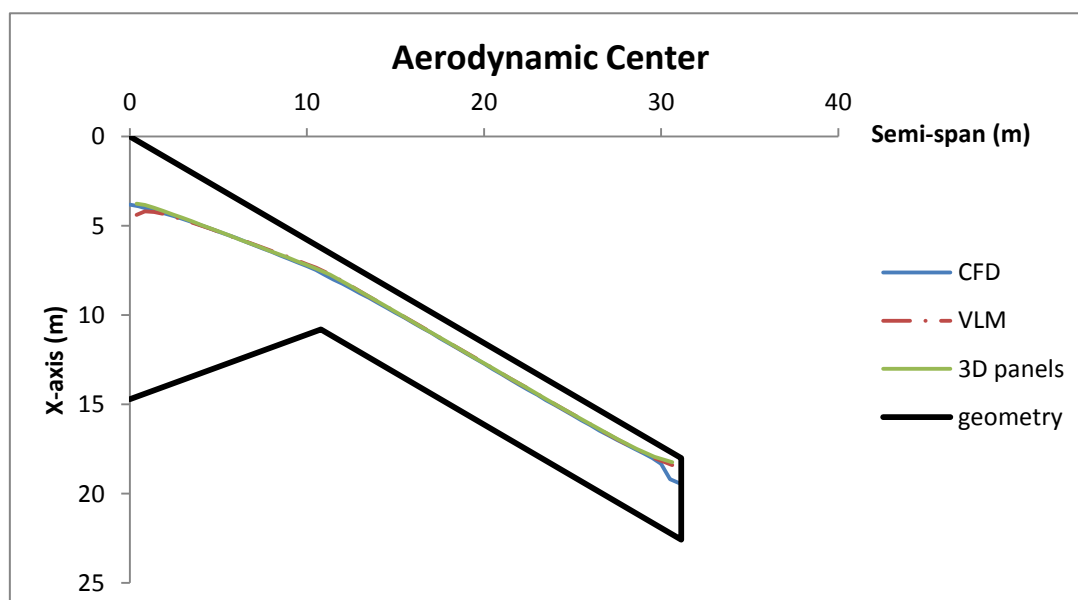
Figure A16: Location of the aerodynamic centre for cruise case

43

As for the gust case, the aerodynamic centre is located very close to the quarter of the chord (cf. Figure A19). The location of the aerodynamic centre moves aft at the tip of the wing. The CFD gives the aerodynamic centre at 34% of the chord, which is due to the tip vortex.

The pitching moment shape does not change between the methods. However, as for the lift distribution, the local pitching moment value decreased by half compared to the gust case (cf. Figure A20). This is explained by the decrease of the dynamic pressure. The density of the air drops from 1.225 kg/m3 at sea level to 0.115 kg/m3 at 60000 ft when velocity is just doubled.
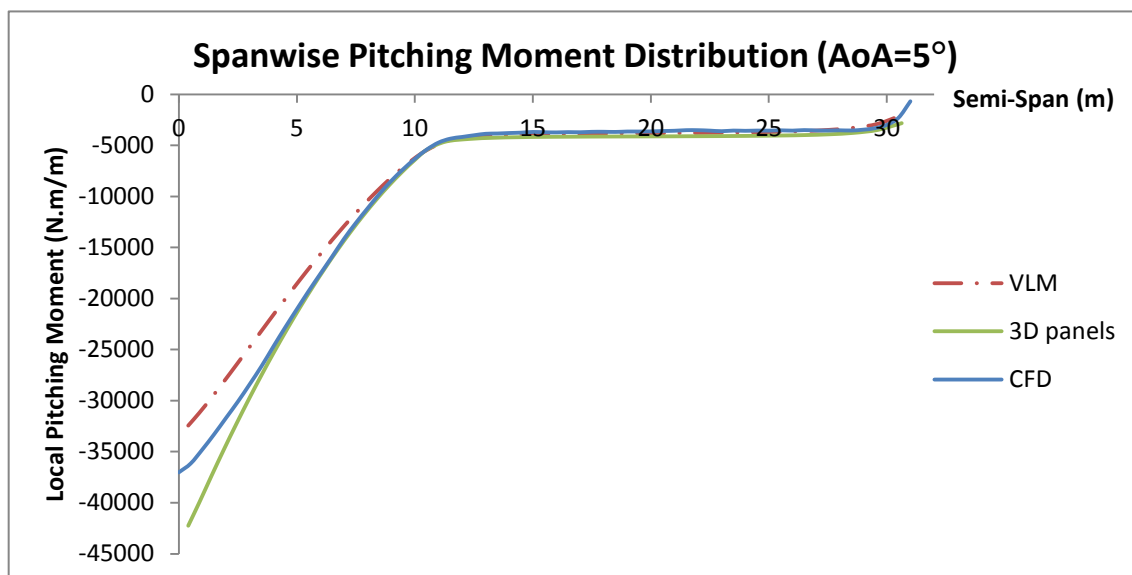
Figure A17: Spanwise pitching moment distribution for cruise case (AoA=0°)

This chapter has compared the results for the lift, pitching moment distribution and the aerodynamic centre. Despite of the assumptions done by the VLM and 3D panels method, the results have shown convergence with the CFD results.

The CFD results have been used for the following load calculations. It would be beneficial study to perform wind tunnel tests to validate the computational results.

44

Appendix B. Mass Estimation and Load Calculation

B.1 Mass Distribution

The mass estimation of the wing consisted in three distinct parts: the structural mass, the system mass and the fuel mass. From the specifications, no detailed data was given on the proportion of the structural mass over the total mass or on the location of the systems. Only the fuel mass was known. The author decided to make assumptions on the different masses and locations of the systems as well as on the structural mass. The procedure adopted to evaluate these parameters is explained in the next chapters.

B.1.1 Structural Mass Distribution

As the system mass distribution was not given, the easiest way to evaluate the structural and system masses was to evaluate the structural mass first.

The wing model was approximated as a rectangular beam representing both front and rear spars, on which the lift is applied. The beam was sized to support the bending due to the lift at ultimate loads.

The height of the beam is the average value of the front and rear spar heights located respectively at 15% and 75% of the chord at the tip of the wing and kept parallel to the leading edge. The layout of the wing structure is described in further details in the next chapter.
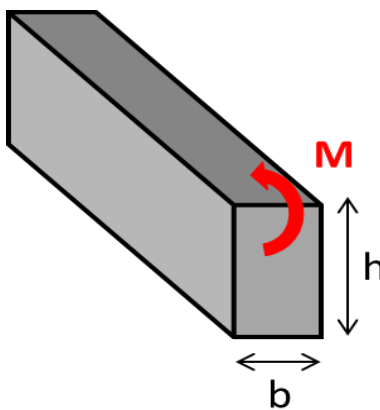
Figure 18: The beam under the bending moment

The thickness of the beam has to be large enough not to fail under loading. The ultimate stress that the beam can support is described by the following criterion:

$$\sigma_{ult} = \frac{Mh}{2I}$$ (B.2)

Where:

- $I = \frac{bh^3}{12}$ is the second moment of inertia of the rectangular beam

- M is the ultimate bending moment

- $\sigma_{ult} = 500$ MPa is the ultimate strength of composite materials, taken as an average value

Section by section, the thickness was computed and the area of the beam was estimated. The mass of the beam was calculated using a density of composite materials of 1600 kg/m^3.
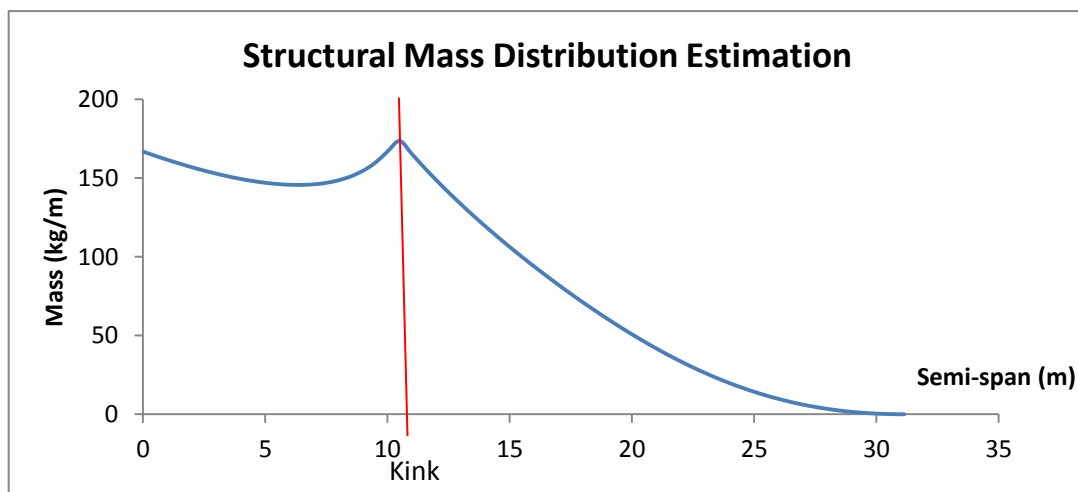
Figure 19: Estimation of the structural mass distribution

The drop of the mass per unit of span at 10.5 m spanwise, i.e. at the kink, is due to the significant increase of the height of the wing box which, consequently, has a higher moment of inertia I.

By integrating this mass distribution along the wing span, a total mass of 5700 kg was estimated for the wing structure.

B.1.2 System Mass Distribution

The system mass was deduced from the structure estimation, by subtracting it from the total empty mass.

Comparing to other aircraft, the engine mass was assumed to be 2 tons per engine, with one engine per side. The engine is located at 5 m outboard from the centreline.

The landing gears weigh 2.2 tons in total (both sides). The main landing gear is considered to represent 90% of the mass and located at 9m from the nose. The nose landing gear is at 1.5 m aft from the datum on the centreline. The location of the engines and landing gears are presented in the Figure 24.
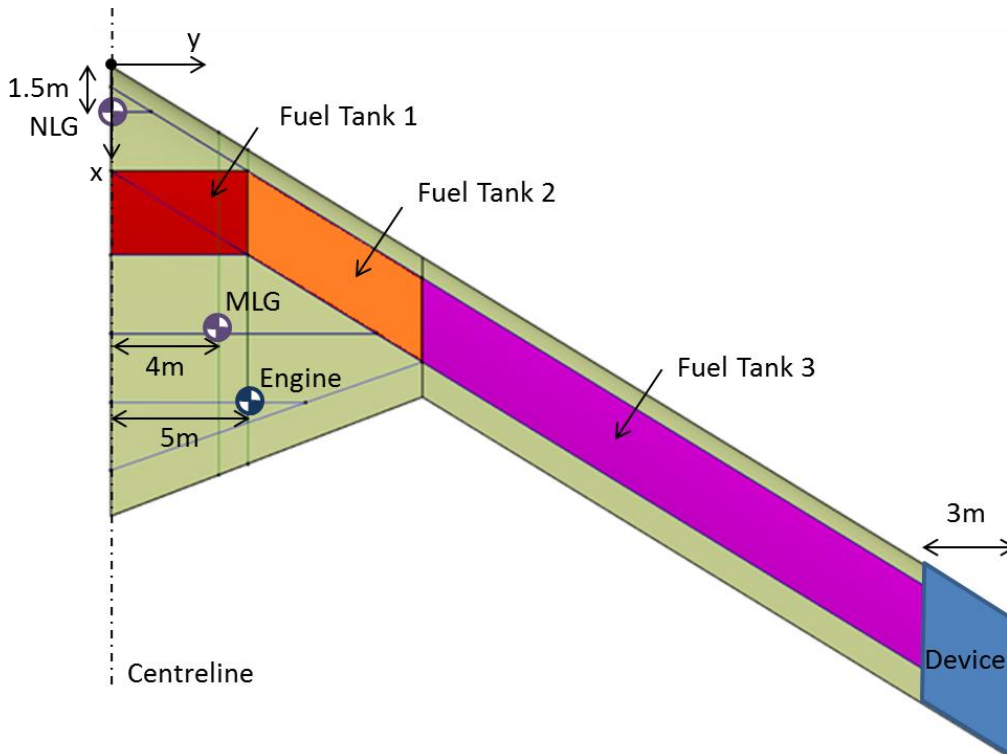
Figure 20: Layout of the main components and fuel tanks

The remaining systems mass consists in the actuation system, fuel and oil pumps, auxiliary power unit, avionics systems…

20% of this mass was distributed from the engine bays to the wing tips for the actuation and fuel system. The other 80% was distributed inboard, between the engine bays. The mass was distributed proportionally to the volume of the cross-sections of the wing.
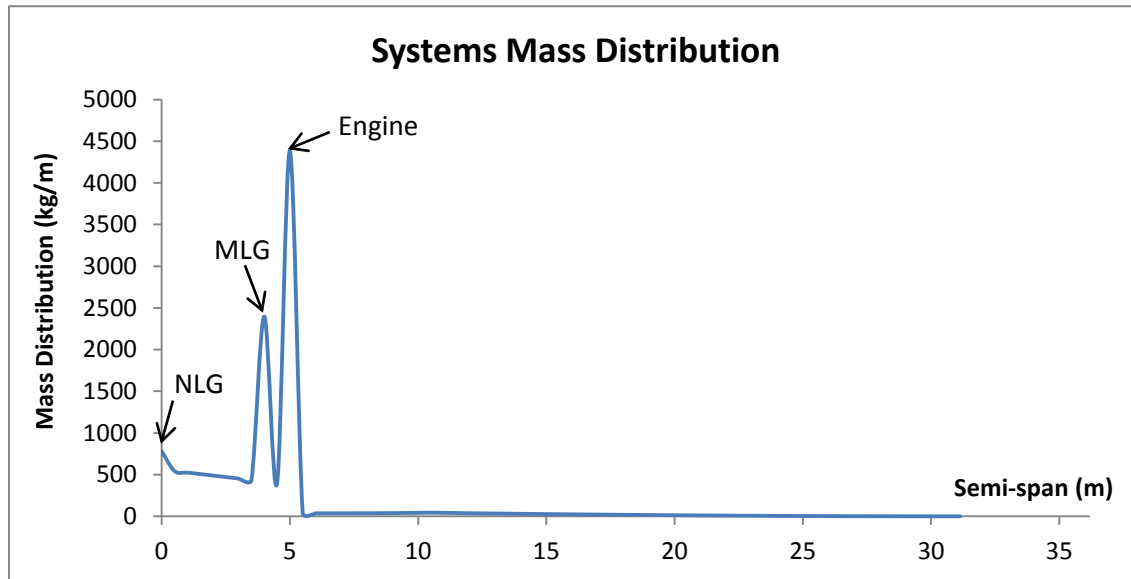
Figure 21: Estimation of the system mass distribution

B.1.3 Fuel Mass Distribution

Several fuel tanks were assumed along the span to fulfill the total fuel mass of 16 tons (for half of the aircraft). The inboard fuel tank 1 (in red in the Figure 24) is delimited by the avionic bay spar. The fuel tanks 2 and 3 are restricted between the front and rear spars. This configuration lets enough space for the systems inboard and permits to have a maximum of load of fuel forward. This choice has been done also to have the maximum of fuel in the front part of the inboard wing to move the centre of gravity forward for stability reasons. The outboard tank 3 is stopped 3 m before the tip of the wing to allow space for the gust alleviation device.

The inboard fuel tank volume is large enough to contain almost all the fuel. Having a maximum of fuel inboard is not the best solution to reduce the loads and bending of the wing. The author preferred to distribute the fuel more uniformly along the span. As a consequence, the inboard fuel tanks are filled at only 25% of their capacity. The outboard tanks are full of fuel, with 20% of the volume measured in CATIA reserved to take into account the structure and systems. The final fuel and total mass distributions are presented in the Figure 26.
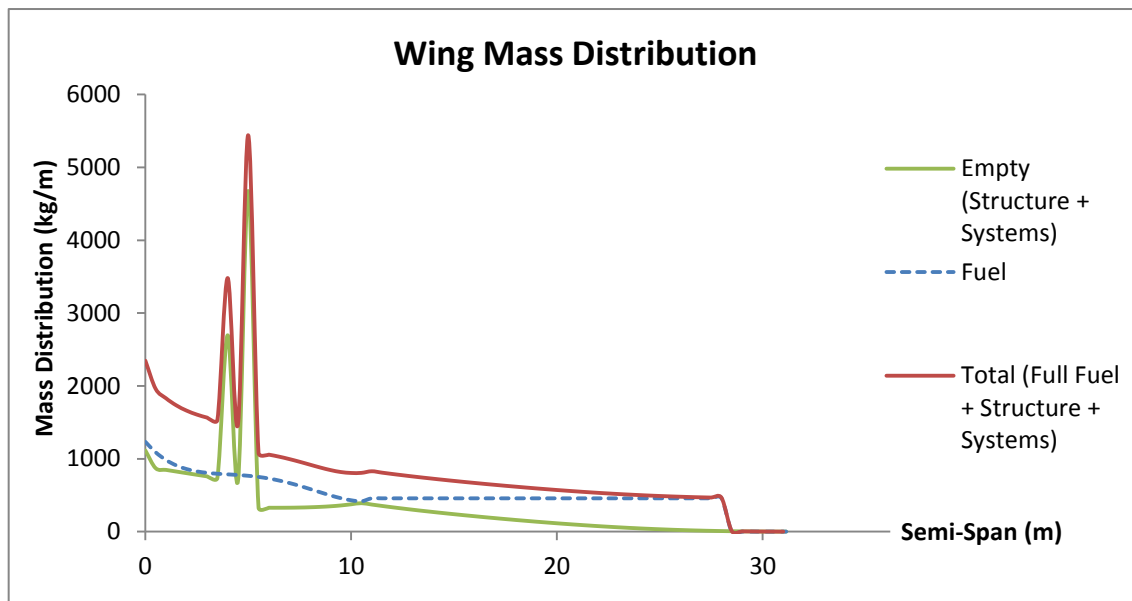
Figure 22: Estimation of the system mass distribution

B.2 Load Calculation

B.2.1 Aerodynamic Data

The data obtained from the CFD was used to compute the loads on the wing. When CFD results were not available, 3D panels results were used instead. This is the case for the gust case at empty weight where an angle of attack of -3° is necessary to balance the weight. The second sea level case needs an angle of attack of -1° from the CFD results.

For the cruise cases, the angles of attack of 5° and 0° has been respectively chosen for full-fuel weight and the empty weight cases to produce enough lift to compensate the weight.

In order to keep the equilibrium of the aircraft, the lift distributions were scaled down to obtain the exact amount of lift needed to compensate the weight.

In real conditions, the angle of attack would be adapted to the conditions to compensate exactly the weight and obtain steady level flight. Furthermore, the lift might be reduced by the deflection of the elevator and other surfaces. The aim of the aerodynamic analyses was to provide the lift distribution shape and confirm that enough lift can be produced by the wing for the different cases.
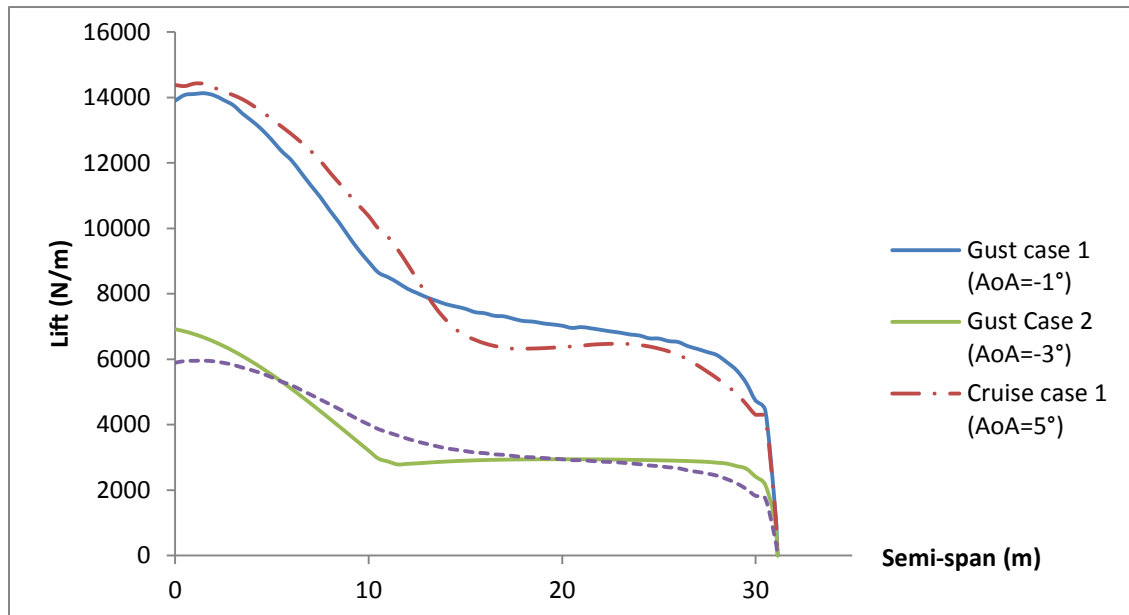
Figure 23: Lift distributions used in the loading actions

B.2.2 Load Factors

The cases studied in this analysis occur at different flight conditions. The maximum load factor the structure can encounter in each situation needs to be calculated to determine the worst loads.

With regards to the span of the aircraft and the take-off mass, the certifications used for the analyses are the EASA CS-25, the certifications for large aeroplanes.

First of all, the flight envelope has to be defined. The maximum load factor n of the flight envelope that the structure has to support is calculated from the equations below:

$$n > 2.1 + \left(\frac{24000}{MTOW+10000}\right) \text{ (MTOW in lb)} \qquad (\textbf{B}.1)$$

And $2.5 < n < 3.8$

This gives a maximum load factor of 2.5 for the flight envelope.

For each case, the gust load factor is determined for initial structural design. The gust load factor was calculated from the alleviated sharp edge analysis presented in the CS-23.

From the article CS-23.333, the gust velocities U_{de} are for each case:

-   Gust case (at sea level): $U_{de} = 50$ ft/s
-   Cruise case (at 60000 ft): $U_{de} = 25$ ft/s

The lift curve slope a_1 was deduced from the aerofoil aerodynamic study done with X-Foil and confirmed with the NACA Report N°832 [26].

The results are presented in the next table:

Table 1: Gust load factor for the study cases

	Gust case 1	Gust case 2	Cruise case 1	Cruise case 2
Gust load factor	2.95	3.81	2.13	3.42

In order to calculate the maximum loads that the structure has to support, the final load factor is chosen between the gust load factor and the flight envelope load factor of 2.5 whichever is the greatest.

B.2.3 Shear Force, Bending Moment, Torque Diagrams

 Once the lift and mass distributions were obtained, the shear force and bending moment were calculated along the span.

 First of all, the convention used in the diagrams is illustrated in Figure 27.

Shear Force   Bending Moment   Torque
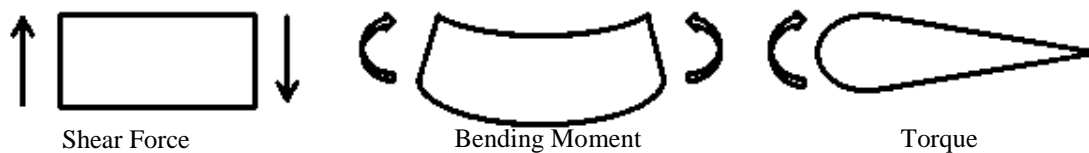
Figure 24: Positive convention for the shear force, bending moment and torque diagrams

 The shear force was calculated section by section, starting by the tip of the wing where the loads are equal to zero. Shear force distributions were first computed for a load factor of 1g.

51
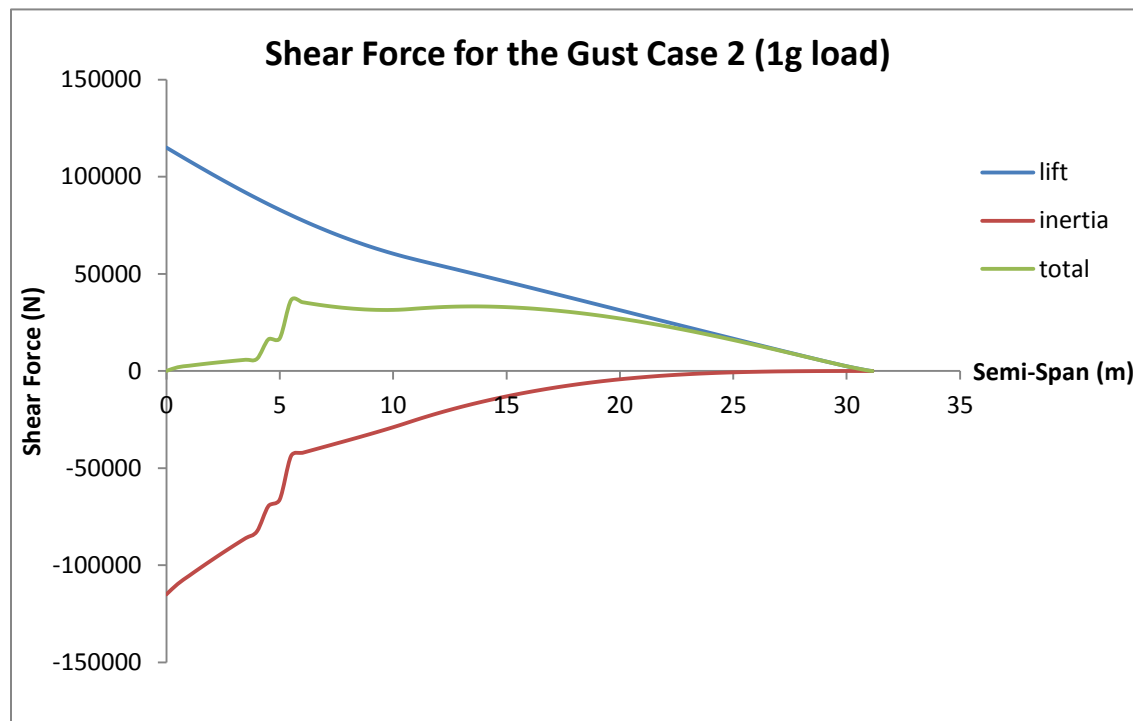
Figure 25: Shear force diagram for the gust case 2 (1g)

Then, the results were multiplied by the load factors calculated previously for the different flight conditions. In the Figure 29, the shear force diagrams for the different cases are plotted at limit load, considering the individual load factors. The shear force starts increasing from the tip where the lift is locally higher that the weight. It can be highlighted that the shear force drops suddenly at 5m for all the cases. This is due to the weight of the engine which is predominant over the lift. Then, the fuel weight and the landing gear weight make the shear force decrease to zero at the centreline, which is expected as the total lift is equal to the total weight. The gust case 2, the gust case at sea level with no fuel, gives the highest shear force for a large part of the span.
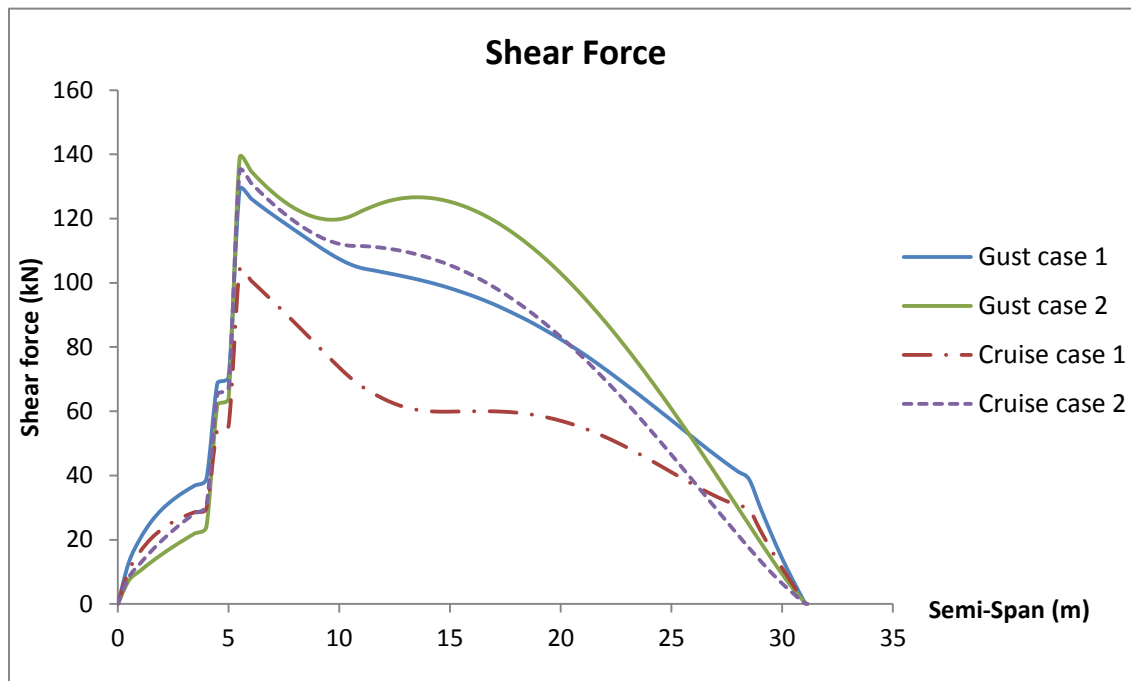
Figure 26: Shear force diagram for the different cases (limit loads)

The bending moment is the integration section by section of the shear force from the tip to the root along the elastic axis. The torque is also calculated on the elastic axis, assumed to be located at 40% of the chord. The moment at the shear centre is obtained from the aerodynamic load and moment at the aerodynamic centre and the weight at the centre of gravity of each section. As the wing is swept, corrections on the bending and torque have to be done to obtain it in the local axis, aligned with the elastic axis [27].

The diagrams for different cases are represented in the Figure 30 and 31. The bending increases gradually to reach its maximum value at the centreline. The gust case 2 is again the worst case with a maximum bending of 4400 kN.m at the centreline. The torque is positive (nose up) from the kink at 10.5 m to the tip because of the correction done to have the values in the local axis. Indeed, corrected torque is calculated with an equation taking into account both non-corrected torque and bending moment values and the sweep angle of the elastic axis. The bending moment is predominant in the equation for this portion so that the final torque becomes positive. Then, from the kink to the centreline, the pitching moment increases significantly (cf. Appendix A) and

creates a nose-down torque. The fuel tanks located upstream in the inboard part of the wing amplify this effect as well. The effect of the aft location on the chord of weight of the engine and main landing gear is observed at 4 m and 5 m of the span by reducing the nose-down torque.
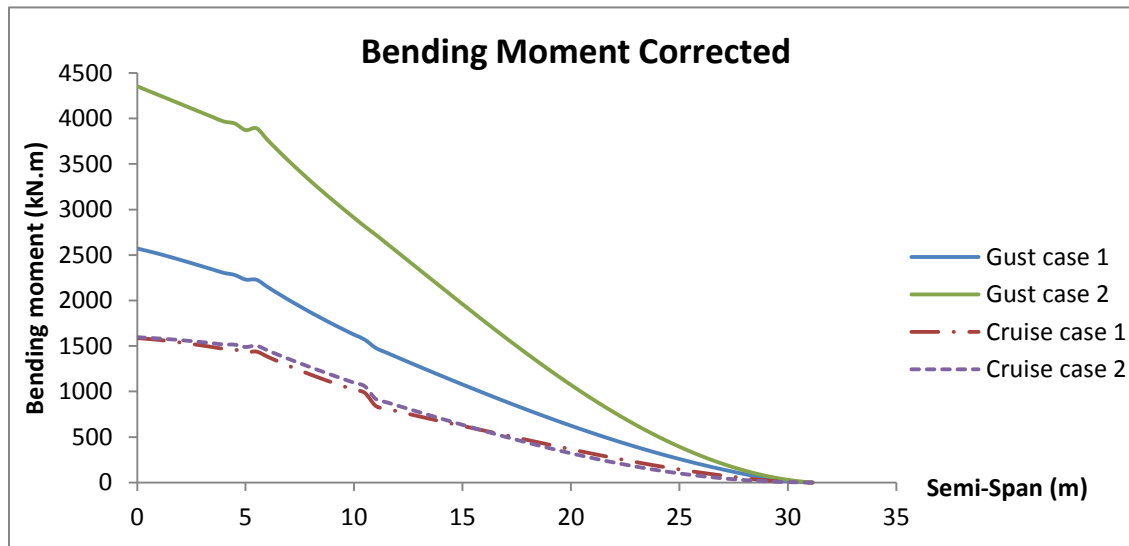
Figure 27: Bending moment diagram for the different cases (limit loads)
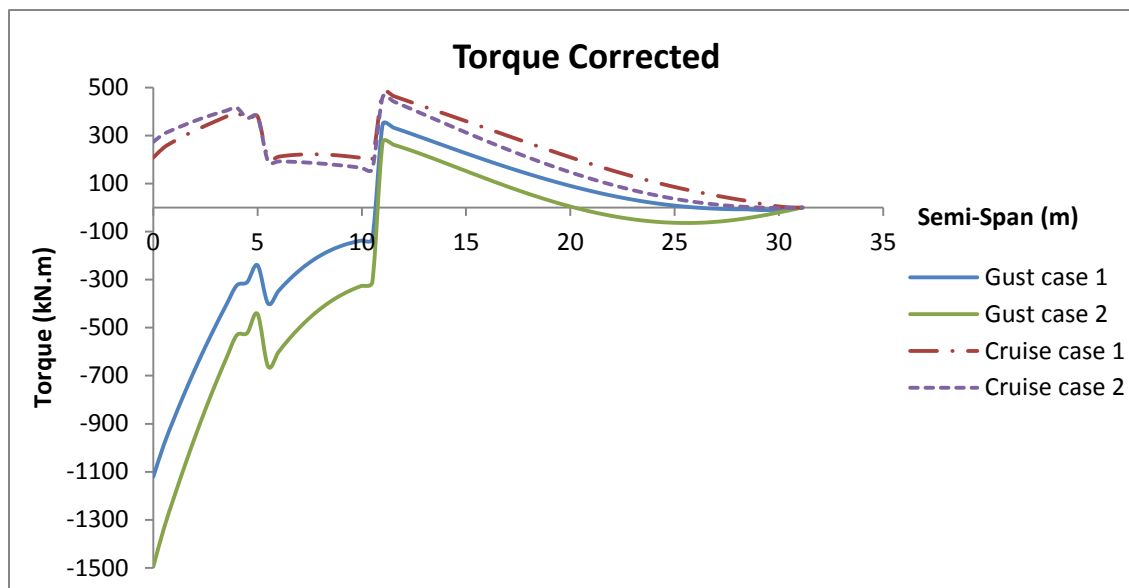
Figure 28: Torque diagram for the different cases (limit loads)

The envelopes of the different diagrams were used for the initial sizing of the structure.

Appendix C. Initial Structural Layout

C.1 General Layout

As briefly presented in the mass distribution chapter, the preliminary design of the flying wing layout has been carried out. The structure aims to support the loads by creating major load paths through the skins, spars, ribs and frames. The total structural weight depends on the configuration and the arrangement of the different members.
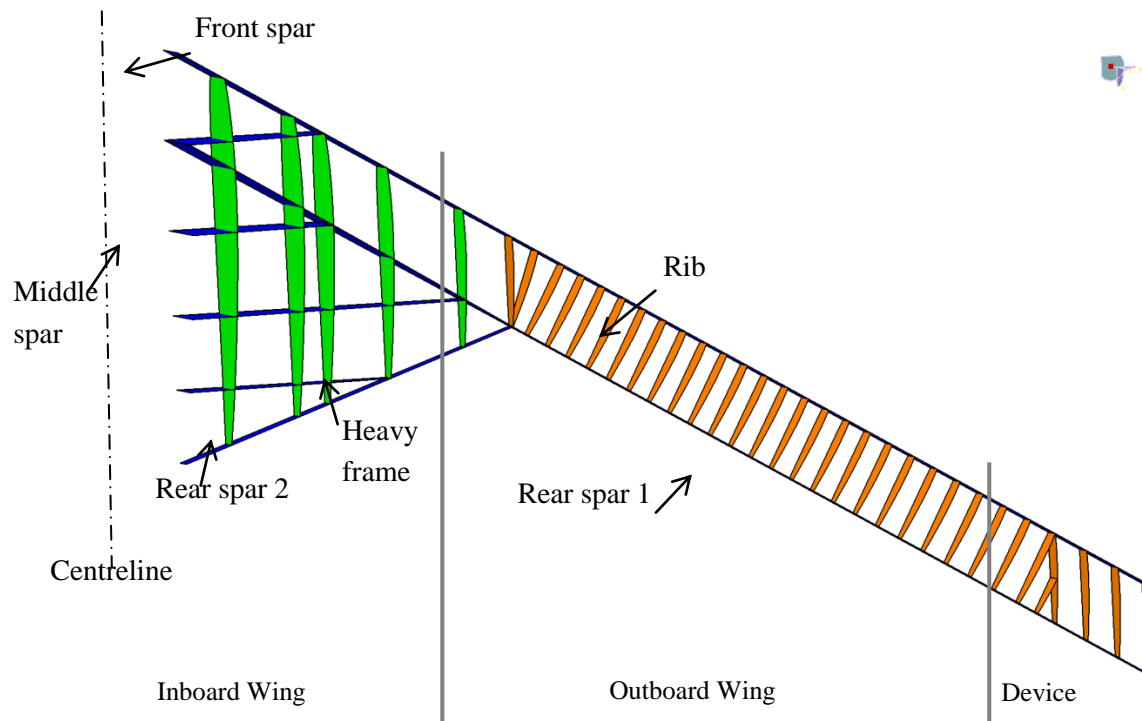
Figure 29: Main components of the structure

The wing can be divided into two distinct parts considering its geometry: the inboard wing and the outboard wing. The inboard wing is constituted of the large tapered central part going to the kink at around 10.5 m laterally. The outboard wing is the straight swept back part from the kink to the tip.

C.2 Outboard Wing

The outboard wing has a conventional two-spar configuration. The front spar and the rear spar are respectively located at 15% and 75% of the chord at the wing tip and are kept parallel to the leading edge / trailing edge along the span. The upper and lower skin are reinforced by I-section stringers to avoid the buckling as high bending moments are applied to the covers creating high compressive loads. For the upper skin, subjected to the highest compressive loads, the stringer pitch has been set to 200 mm, following the typical values in aircraft design [13]. Contrary to the upper skin, the compressive loads are lower for the bottom skin as the design case is the bending due to the weight of the wing (1g case). In the objective of weight reduction, the stringer pitch has been increased to 400 mm for the lower skin from the section 8 to the tip (cf. Figure 34). A balance between the number of stringers and the skin thickness has been defined to have proportional dimensions between the skin and stringers designs. The skin also needs a minimum thickness regarding lightning protection. The ribs are perpendicular to the rear spar to give the best arrangement in terms of load transmission from the trailing edge devices. The rib pitch is set at 750 mm at the kink and increased progressively to 1 m at the tip of the wing, where the loads are lower.

The tip of the wing has been considered separately in the design phase to take into account the future presence of the passive gust alleviation device. The last three meters are reserved for the device design. The front and rear spars are kept at the same emplacement but the rib direction is changed for the streamline direction. This choice has been motivated by the absence of trailing edge devices and the fact that the device rotates around the shaft in the y-axis. As the bending and torque at the tip are low, the stringer pitch has been increased to 400 mm for both upper and lower skin.
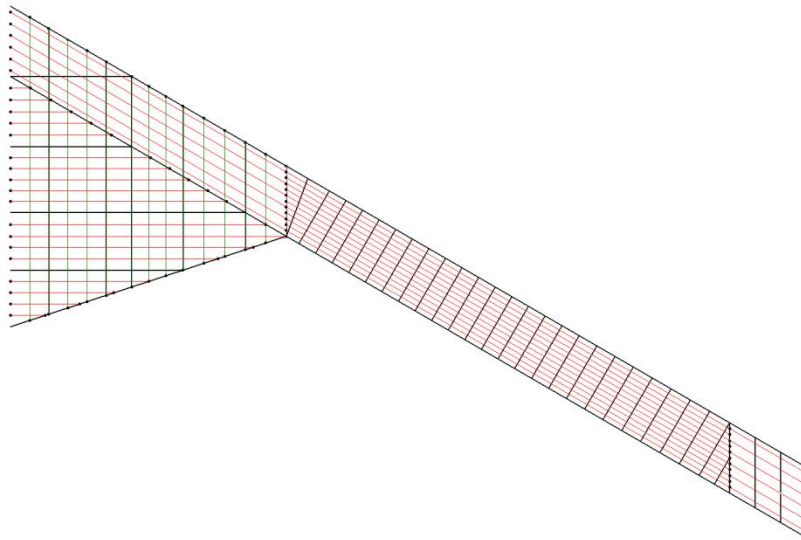
Figure 30: Upper skin layout

C.3 Inboard Wing

The inboard wing is composed of numerous elements. With its triangular shape, a conventional wing design cannot be applied in this case. The loads are coming for the outboard part of the wing through the front and rear spars and the stiffened skin panels.

In order to keep continuity of the load paths, the stringers follow the same direction and shape as the inboard part. Since the height of the wing box increases significantly from the kink to the centreline (0.5 m at the kink to 1.5 m at the centreline) and the applied compressive loads are inversely proportional to the wing box height, the skin panels do not need to be as stiff as the outboard skins. Thus, the stringer pitch has been increased to 400 mm for both upper and lower covers, reducing the weight of the covers. The front and rear spars of the outboard wing come through the fore part of the wing. Additional spars called 'middle spars', are located in the centre of the wing. They separate the inboard wing, delimit the fuel tanks and help supporting the spanwise shear force, the engine and landing gear masses (cf. Figure 24). A 'second rear spar' comes from the kink and follows the trailing edge to give a support for the control devices and flaps. Frames are designed to support the chordwise bending. The heavy frames are constituted of a web and I-section caps attached to the upper and lower skins. They support the chordwise

bending as well as the chordwise shear. They have the same function as the ribs and help supporting the heavy mass of the systems such as the engines. The light frames, set as chordwise stiffeners, are placed between the heavy frames to protect the skin against buckling. The light frames are I-section beams uniformly spaced of approximately 750 mm between the heavy frames. They are boundaries for the spanwise stringers.

Appendix D.   Initial Sizing

D.1 Material Selection

The selection of the material is an important decision to make as it has a direct impact on the structural design and stress analysis and thus on the weight of the structure. Weight saving is the first concern of all aircraft designers to reduce the fuel consumption, increase the maximum range and the payload. Aluminium alloys have been the most chosen for several decades; their properties have been improved over time. However, the composite materials take an increasingly important role in the structure materials.

The composite material's reduced density is the one of the advantages of these materials compared to the aluminium alloys but their anisotropic properties make the design complex. For a flying wing, the high tensile performance of the CFRP laminates is ideal for the skin design which is subject to high bending. The laminate layup has to be tailored to the main load paths of each component to maximize the benefits of the use of the composite materials. The bending-torsion coupling properties of the laminate can be adapted to improve the aeroelastic behaviour, the structural modes of the wing. The composites present also a longer fatigue life which allows either to delay the regular inspections or to reduce their number.

The common 8552 epoxy matrix IM7 UD carbon fibre, an intermediate modulus carbon fibre epoxy matrix composite has been chosen for the whole flying wing. The properties of the material are presented in the Table 4.

Table 2: 8552/IM7 Material properties [28]

0° tensile modulus	GPa	E_1	164
90° tensile modulus	GPa	E_2	12
Shear modulus	GPa	G_{12}	5.8
0° tensile strength	MPa	X_t	2724
90° tensile strength	MPa	Y_t	111
Shear strength	MPa	S	120
0° compressive strength	MPa	X_c	1690

90° compressive strength	*MPa*	Y_c	250
Poisson ratio	-	v_{12}	0.3
Density	*g/cm³*	ρ	1.57
Ply thickness	*mm*	t	0.131
Fibre volume	*%*	V_f	57.7

Once the material was chosen, the initial sizing of the different wing components was fulfilled. These component sizes were then input in the Finite Element program to analyze the structure.

D.2 Member Initial Sizing

D.2.1 Introduction

The member initial sizing was derived from the shear force, bending moment and torque diagrams. The worst loads from the four cases studied in the Chapter 4 were used to calculate the local stresses in the structure members. The geometric data needed for the calculations, such as the wing box height, the rib pitch, were obtained from CATIA.

The laminate engineering properties were derived from CoALA [29] , an in-home software, in which the laminate plies were input. The stiffness matrices are also computed. This software calculates the failure indices and strains of each ply of the laminate for a given load. The failure indices were checked to be below one under ultimate loads (limit load x 1.5). The strains were kept under 3500 με at limit loads for damage tolerance.

The laminate layups chosen are all balanced and symmetric. In order to keep an acceptable number of layup combinations, only 0°, 90° and +45°/-45° angles were used for the ply direction. Typical laminate layups are defined for the components. They are repeated to obtain the desired thickness of the components.

The laminate design followed the usual guidelines:

- A minimum of 10% of plies in each of the four directions

- No 0° and 90° consecutive plies

- A maximum of four consecutive plies of the same direction

- +45°/-45° directions used for the exterior plies for damage tolerance

In order to facilitate the sizing, design sections have been created along the wing span. The following initial sizing of the components is based on this section division.
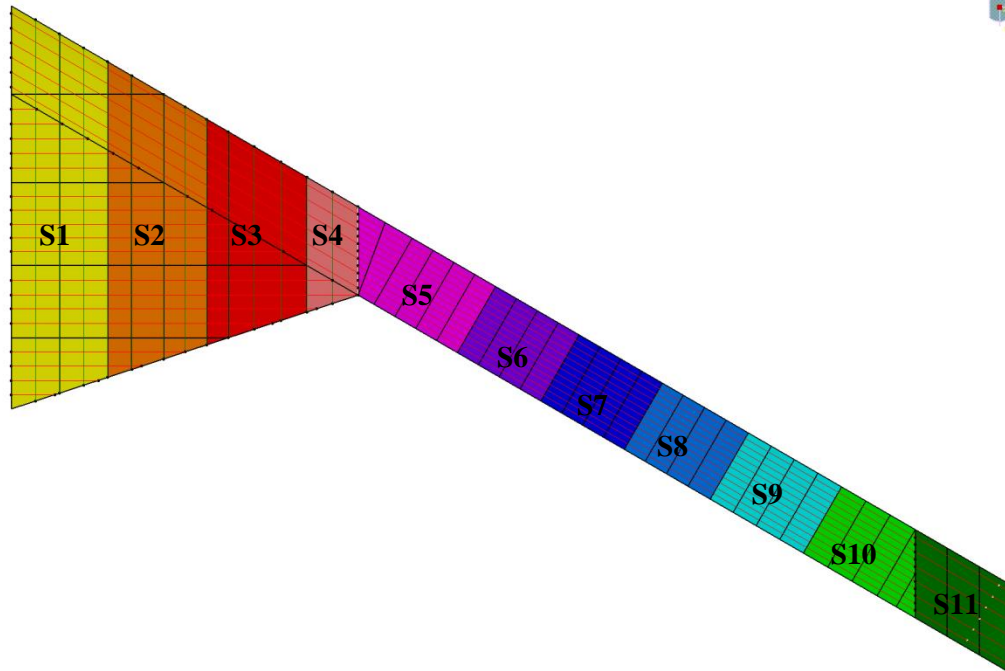
Figure 31: Sections for the initial sizing

D.2.2 Skin / Stringers

The upper and lower surfaces are subject to high spanwise bending moments. Consequently, the upper skin is reinforced by I-stringers to support the compressive stresses.

In order to simply the initial sizing analysis, a single laminate layup [+45/02/-45/90]s was used for both skin and stringers. 0° plies need to be in major proportion in the skin layup to support the axial loads but also, a non-negligible percentage of +45°/-45° plies is needed for the shear induced by the torque around the wing box.

The stiffened panels were designed to resist buckling and keep the strains under the limit of 3500 $\mu\varepsilon$. The ultimate bending moment obtained from the loading actions was used for the upper surface buckling design and the limit loads for the strain design for both upper and lower surfaces. The lower surface is in compression when the aircraft is on the ground. Thus, the bending due to

the wing weight (1g load) was computed to determinate the compression loads and to size the lower stiffened surface.

The load applied to the skin/stringers for each section is determined by:

$$N_x = \frac{M}{wh} \qquad \text{(D.1)}$$

Where N_x is the edge load applied to the skin/stringers panel, M is the bending moment, h is the height of the wing box and w is the width of the wing box.

This analysis was conducted by V. Fu who determined the best design for the skin and the stringers at each section using an in-house code.

Table 3: Skin panels thicknesses

Section	Upper skin thickness (mm)	Lower skin thickness (mm)	Section	Upper skin thickness (mm)	Lower skin thickness (mm)
1	4.45	3.67	7	5.24	3.41
2	5.24	2.88	8	4.72	3.93
3	6.03	3.14	9	4.19	3.41
4	7.60	5.24	10	3.14	2.62
5	6.29	4.45	11	2.10	2.92
6	5.76	3.93			

D.2.3 Spars

The spar web is designed to support shear. From the beginning, the layup [+45/0/-45/90]S was chosen for its fifty per cent of +45/-45 plies resisting the shear. The shear is calculated from the worst values of shear force and torque in the wing box. The spar configuration is quite complex in the inboard part of the wing where there are up to seven spars at the section. The initial sizing of the spar web was first achieved for the outboard part where a simple front and rear spar configuration exists.

The following equations were used to determine the shear flow in the front and rear spar web. The shear forces applied to the front and rear spar are:

$$F_{FS} = \frac{V h_{FS}{}^2}{h_{FS}{}^2 + h_{RS}{}^2} \ and \ F_{RS} = \frac{V h_{RS}{}^2}{h_{FS}{}^2 + h_{RS}{}^2} \qquad \text{(D.2)}$$

Where V is the shear force applied at the section and h_{FS} and h_{RS} are the height of the front and rear spars respectively.

The shear flow in the web due the shear force is:

$$Q_{V,FS} = \frac{F_{FS}}{h_{FS}} \ and \ Q_{V,RS} = \frac{F_{RS}}{h_{RS}} \qquad \text{(D.3)}$$

The torque creates also a shear flow around the wing box in addition to the above shear flow in the spar web.

The shear flow due to the torque is:

$$Q_T = \frac{T}{2A} \qquad \text{(D.4)}$$

Where T is the worst value of the torque at the section and A is the area of the wing box cross-section.

Because of the orientation of the shear flow in the spar webs, different values of the torque have been used. As presented in the Figure 35, the maximum positive torque value is used for the front spar whereas the maximum negative torque is applied to the rear spar.
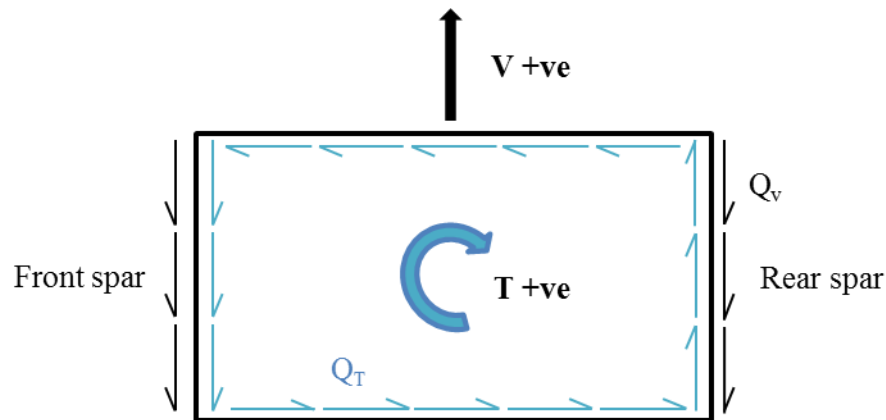

Figure 32: Simplified shear flow diagram in the wing box

The total shear flow applied to the front and rear spar webs are:

$$Q_{FS} = Q_{V,FS} + Q_{T,positive} \ and \ Q_{RS} = Q_{V,RS} - Q_{T,negative} \qquad \text{(D.5)}$$

Then, the different sections of the outboard wing were sized by applying the previous shear flows to the laminate in CoALA [29] and checking the failures indices and strains.

The thicknesses of the front and rear spar webs are presented in the Table 6.

Table 4: Front and rear spar web thicknesses of the outboard wing

Section	Front Spar Web Thickness (mm)	Rear Spar Web Thickness (mm)
5	6.03	2.88
6	5.50	2.88
7	4.98	2.62
8	4.45	2.36
9	3.41	1.83
10	2.36	1.31
11	1.57	1.05

Regarding the inboard sections, the increasing torque might be balanced by important depth of the wing box and the drop of the shear force. Since the front spar carries most of the shear in the outboard wing, the thickness of the web has been kept to 3.93 mm for the sections 3 and 4 which are the most critical of the inboard wing in terms of shear. The remaining part of the front spar and the other spars of the inboard wing have a web thickness of 1.83 mm.

The spar caps are the components making the link between the spar web and the skin surfaces. They can be compared to stringers as they support mainly bending. The layup [+45/02/-45/90]s, same as the skin/stringer, and T-section beams were chosen for the design. Due to time constraints, it has been assumed that the dimensions are double the stringers dimensions.

64

D.2.4 Frames

Heavy Frames

The heavy frames were sized to support the chordwise bending. They support compression from the spanwise torque, which, in the chord direction, is equivalent to the bending. The caps are designed using Euler buckling analysis. The layup used is the same as for the stringers, [+45/02/-45/90]s, to resist the compressive loads.

The method followed is iterative; several designs have been tested to find the appropriate design. First of all, the applied loads are defined. The compressive load is derived from the spanwise torque from the loading actions:

$$P_{compressive} = \frac{T}{2A} \times L \qquad (D.6)$$

Where T is the ultimate spanwise torque at the section, A the total wing box area and L is the length of the frame.

The applied stress on the section is then calculated:

$$\sigma_{applied} = \frac{P_{compressive}}{A_{frame}} \qquad (D.7)$$

The Euler buckling allowable stress is computed following the equation [30]:

$$\sigma_{CR} = \frac{\pi^2 E I_{NA}}{A L^2} \qquad (D.8)$$

Where E is the tangent modulus of the material, here assumed to be equal to the elastic constant E_{11} derived from CoALA, I_{NA} is the second moment of inertia about the neutral axis, A is the area of the cross-section of the beam and L is the length of the beam.

Light Frames

The light frames can be considered as "chordwise stringers". They are designed in the same way. The compressive loads applied between the heavy frames are calculated the same manner as for the heavy frames. The layup of the I-section light frames is also the same as the stringers and the heavy frames: [+45/02/-45/90]s. The skin/light frames are sized with the automated code used for the skin/stringers buckling design. The thickest skin between the light frame and stringer skin design is finally retained for the final section skin thickness.

65

Appendix E.   Static Finite Element Analysis

FEA (Finite Element Analysis) is a computational method to calculate the structural behaviour under specified conditions. The FEA is commonly used in research departments to evaluate the structure strength before testing it with expensive experiments. FEA is nowadays a key step in the structural design.

In the framework of the thesis, the wing was modelled and constrained under loads with the pre-processor Patran. The analyses are run by the finite element calculator Nastran.

In this chapter, the static linear analysis of the half of the wing is presented. Further analyses of the structure modes and dynamic response are described in the later chapters.

Because FEA can be a time-consuming task, the author built the model step by step to avoid numerous problems. A mesh sensitivity analysis has been conducted to evaluate the reliability of the results of the static analysis in function of the mesh size.

E.1 CATIA Surface Model

The geometry of the wing was constructed in the software CATIA. The skins, spar and heavy frame webs and ribs were represented by surfaces. The beams, such as the stringers, spar caps and frame beams were symbolised by lines. All the surfaces were cut by the spar, rib, frame and stringer planes to permit an easier mesh in Patran. The surface model was imported into Patran using the Parasolid import function for the STEP files from CATIA. The inboard, outboard and device part were separated into different groups to allow later changes in the device design for example. The final surface model counts 1922 surfaces for half of the aircraft.
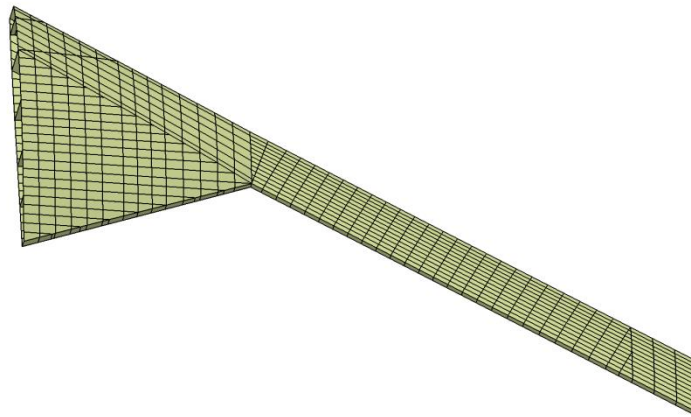
Figure 33: Surface model from CATIA

E.2 Mesh

A mesh sensitivity analysis has been conducted to evaluate the influence of mesh element size on the results. Three different meshes were built in Patran, by increasing the number of mesh elements by approximately two between each mesh. The number of elements and nodes is given in the Table 7.

Table 5: Mesh nodes and element numbers

	Mesh 1	Mesh 2	Mesh 3
Nominal element edge length (mm)	200	150	100
Number of Elements	19169	29657	63130
Number of Nodes	11010	19334	47106

The meshes of the surfaces use mainly Quad4 elements with the IsoMesh function. In the other cases, Tria3 elements were used and paver and hybrid options were chosen when the surfaces were not rectangular and impossible to be meshed with IsoMesh function.

To ensure that the elements are all connected together, mesh seeds were used for the edges. Equivalence of the nodes has been completed and free edges have been checked. The verification function of the elements in Patran was used to check the dimensions of the Quad and Tria elements (aspect ratio<5, skew angle>30 for quad, skew angle>10, taper<0.5 and warp angle<0.05 for quad).

67

The stringers, frames and spar caps were meshed by bar elements along the lines of the surface model.
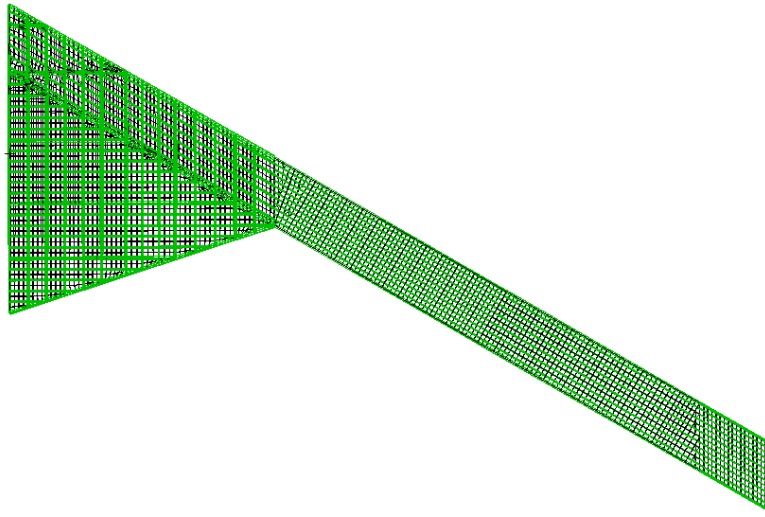

Figure 34: Mesh 1

E.3 Properties

The material properties were input into the software. In the first approach, an equivalent aluminium alloy was used to check that the meshes have not got any errors. Then the properties of the 8552/IM7 UD composite prepreg were entered into the software as a 2D orthotropic material. The layups of the laminates were defined for the components, following the choices done during the initial sizing. The shell properties for the skins, ribs, frame webs and spar webs as well as the beams dimensions for the stringers, frames and spar caps were attributed to the mesh elements.

E.4 Boundary Conditions and Loads

The model input in Patran is the half of the aircraft. To represent the boundary conditions at the root section, the nodes on the edges at the centreline were fixed, constraint in both translation and rotation.

The loads applied on the structure were derived from the previous aerodynamic results. Unlike the initial sizing where shear, bending and torque need to be calculated to size the components, the FE model only needs the aerodynamic loads. Indeed, the results of loads into bending moments are

part of the calculation of the software. The mass of the structure is also taken into account by the application of an inertial load.

The worst load case in terms of bending was used for the analysis. This is the case at sea level at empty weight for a static gust load factor of 3.81g (gust case 2). The aerodynamic loads applied in the model are derived from the lift distribution obtained during the aerodynamic analysis. The lift and the pitching moment are distributed along the span by idealising it in punctual loads. The loads are applied on the nodes located at the aerodynamic centre of the frame and rib webs.

The inertia of the components is considered by the application of an inertial load of 3.81g to the whole structure.

Figure 38 presents the total load distribution and boundary condition applied on the model.

Wing root clamped

Lift and pitching
moment at the AC

Inertia
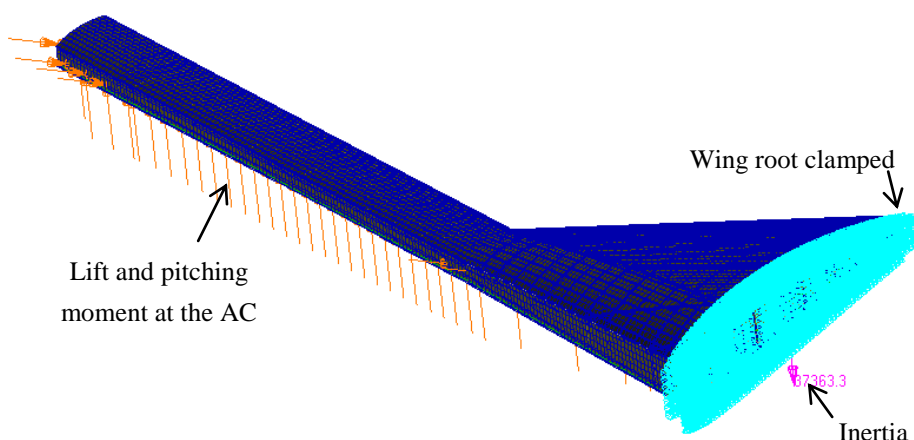
Figure 35: Loads and boundary conditions applied on the model

E.5 Static Analysis Results

Once the model was completely built, a static linear analysis was performed by the solver Nastran for each of the three meshes.

E.5.1 Results for the Mesh 1

Figure 39 presents the displacement of the wing under limit loads. The wing tip reaches a maximum displacement of 2.56 m. This value demonstrates the flexible characteristic of the flying

wing, but it needs to be put in perspective with the fact that it is obtained for the load factor of 3.81g.

Max displacement : 2560 mm
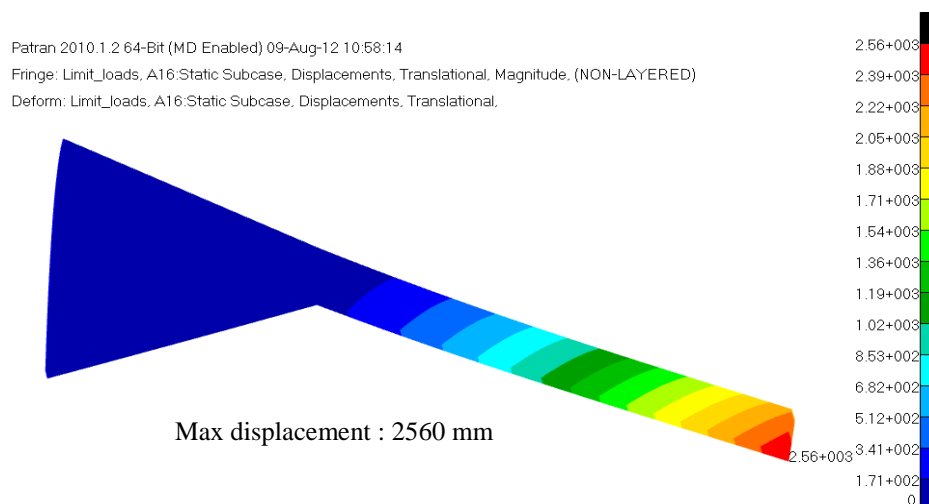
Figure 36: Displacement of the structure under limit loads

The failure indices (FI) and the strains of the members preliminary sized were computed to verify that they are under the design limits. The Twai-Wu failure criterion was used for the calculation of the FI.

It can be seen in Figure 40 that the FI do not exceed the value of 0.56 in the upper skin. The strains are plotted as minimum principal strain because the upper skin supports mainly compression loads. The maximum magnitude of the strains reaches 3320 $\mu\epsilon$ which is under the limit of 3500 $\mu\epsilon$ established at the beginning of the study (Figure 41). It can be observed that the main strains and stresses are located around the kink, in the outboard part, where the loads are high and the structure thin.

Patran 2010.1.2 64-Bit (MD Enabled) 09-Aug-12 10:41:32
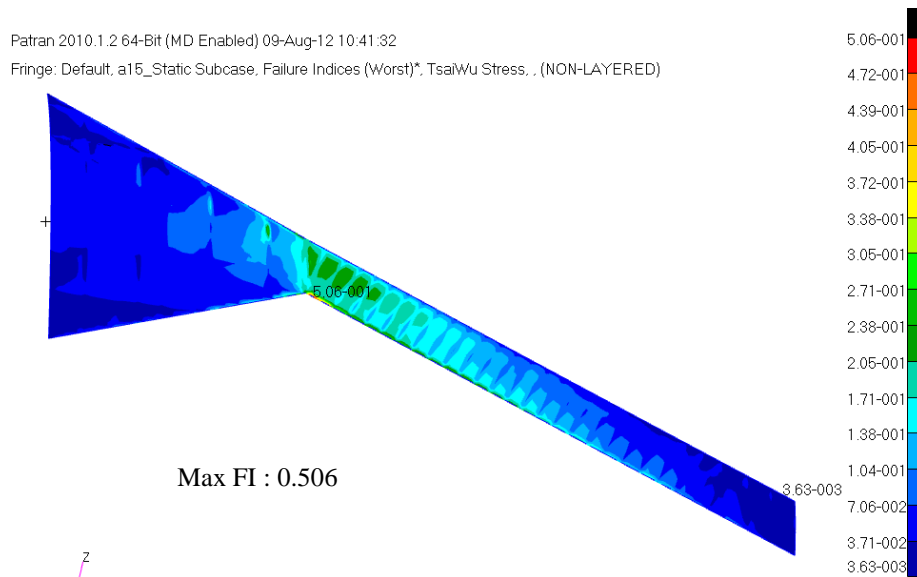Fringe: Default, a15_Static Subcase, Failure Indices (Worst)*, TsaiWu Stress, , (NON-LAYERED)

Max FI : 0.506

Figure 37: Upper skin FI

Patran 2010.1.2 64-Bit (MD Enabled) 09-Aug-12 10:56:44
Fringe: Limit_loads, A16:Static Subcase, Strain Tensor, , Min Principal, 58 of 58 layers (Maximum)
Deform: Limit_loads, A16:Static Subcase, Displacements, Translational,

Max strain : 3320 με
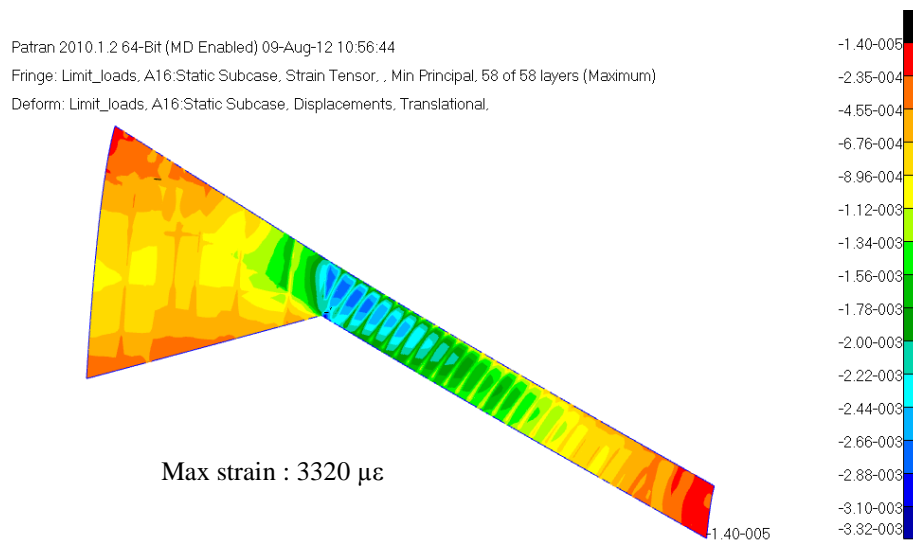
Figure 38: Upper skin strains

The lower skin is under tensile loads. The FI, illustrated in the Figure 54, stay under one with a maximum value of 0.81. However the strains are critical for the design of composite structure. The design limit of 3600 με is exceeded at the kink with a maximum strain of 5200 με (Figure 43). The stresses at this concentration area must be reduced to avoid too high strains for damage tolerance considerations. After verification that this concentration of loads is not due to the mesh,

71

the thicknesses of the components in this region were increased to have the strains under the design limit.

Max FI : 0.811
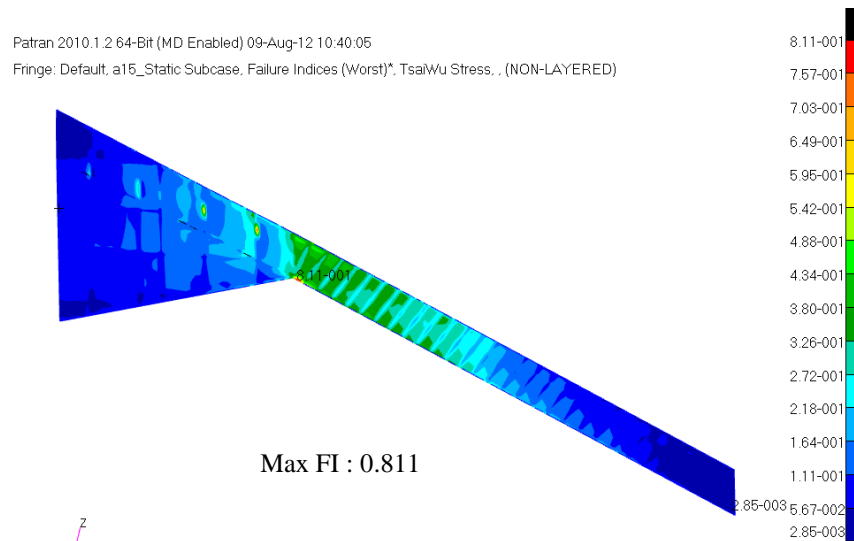
Figure 39: Lower skin FI

Max strain : 5200 µε
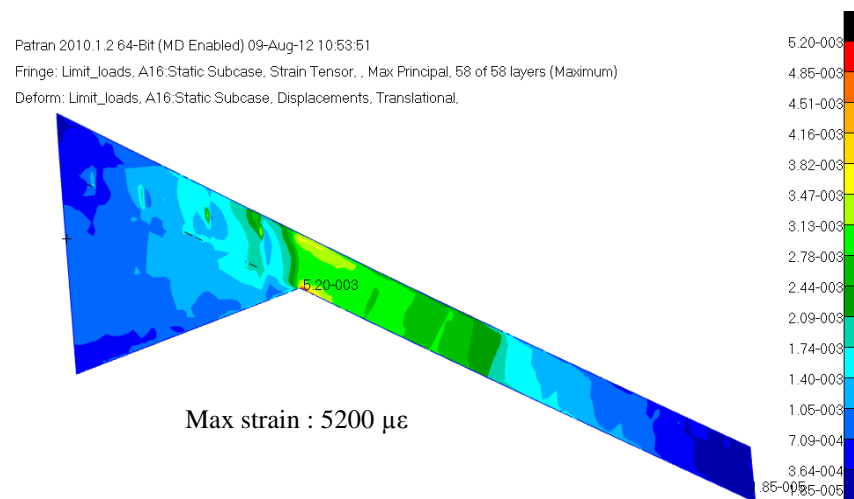
Figure 40: Lower skin strains

The spars FI and strains are also checked. Excluding the concentration points in the inboard spars due to the application of punctual loads in the model, the same issue as the lower skin is encountered for the rear spar at the kink. Although the maximum FI is 0.86 at this location (Figure 44), the strains reach the upper value of 5200 µε. In the same approach as for the lower skin, the thickness of the rear spar was increased.

72
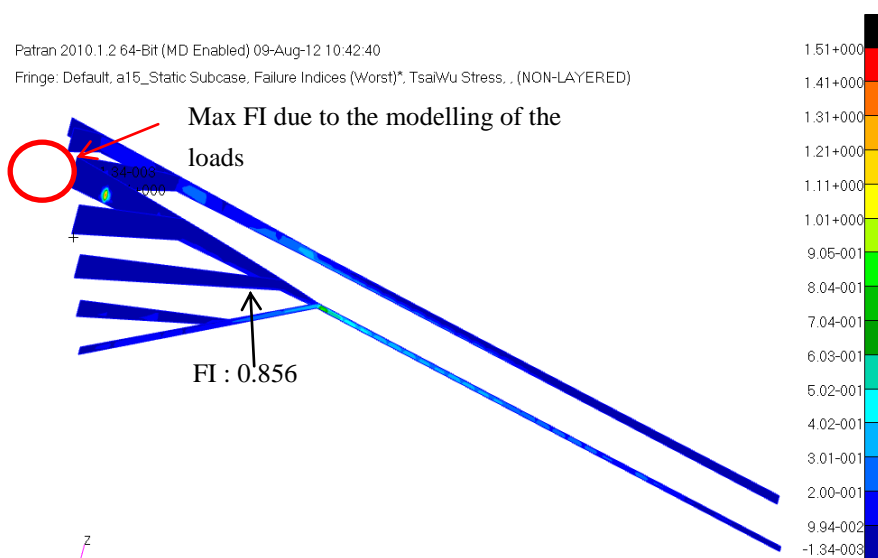
Figure 41: Spar FI
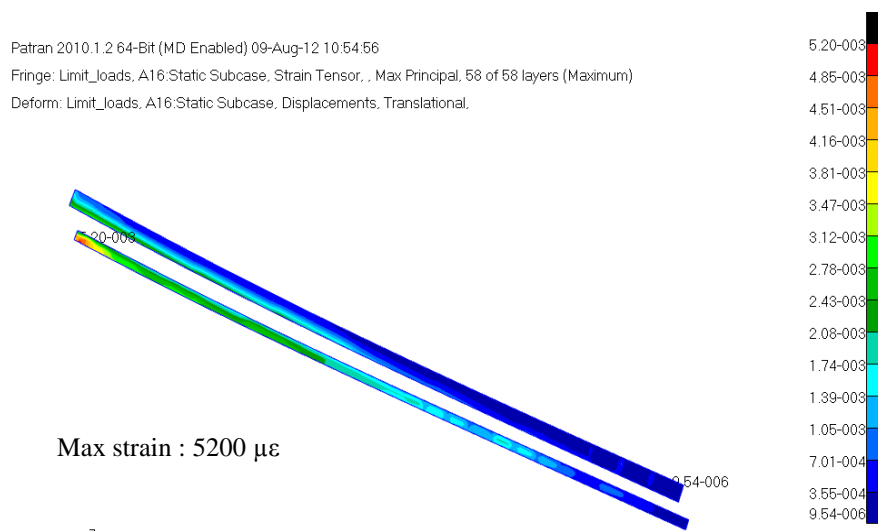
Figure 42: Outboard spar strains

E.5.2 Mesh Sensitivity Study

This is a primary concern to ensure that the results obtained by the FE model are reliable. The mesh sensitivity analysis is used to verify that the results are not a function of the spatial discretisation of the model. The results presented above from the first mesh can be compared to the results obtained with the two finer meshes. The deflection of the wing, the FI and strains for the components were calculated for each of the meshes. The results are presented in the Table 8.

73

Table 6: Comparison of the results between the meshes (worst values)

	Mesh 1 (coarse)	Mesh 2	Mesh 3 (finest)
Deflection (limit loads)	2.56 m	2.56 m	2.55 m
Upper skin FI	0.51	0.52	0.53
Upper skin strains	3320 με	3160 με	3520 με
Lower skin FI	0.81	0.79	0.91
Lower skin strains	5200 με	5050 με	4700 με
Outboard rear spar FI	0.86	0.86	0.92
Outboard rear spar strains	5200 με	5050 με	5250 με

In the Figure 46, it can be seen that the results from the three meshes are quite convergent. If mesh 3, the finer mesh, is taken as the reference, the maximum difference between the values is 13% for the lower skin FI between the meshes 2 and 3.

Therefore, the results obtained with the mesh 1 can be considered reliable enough considering the assumptions done in terms of modeling of the loads. This mesh will be used for the further finite element analyses which demand a higher amount of calculations and computational resources. The optimization process also limits the number of mesh elements.
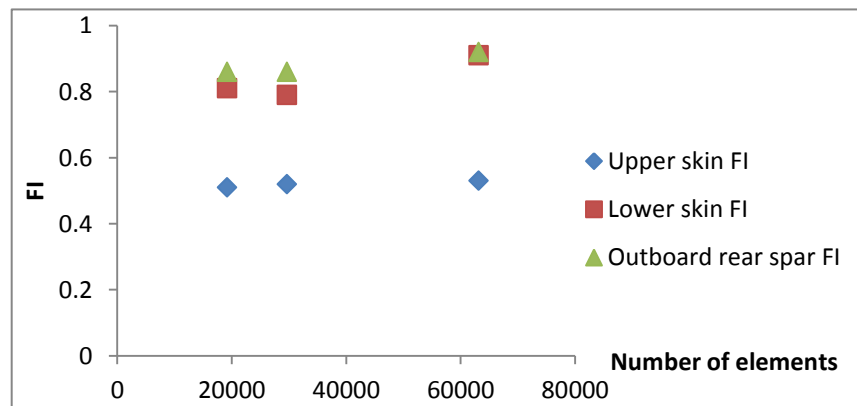
Figure 43: FI results in function of the number of mesh elements

E.5.3 Update of the Structural Component Dimensions

As presented earlier, the strains in the lower skin and outboard rear spar at the kink are exceeded. In order to reduce it to the design limit, the thicknesses of the components of the design section 5 have been increased progressively. The dimensions of the lower skin and rear spar are given in the Table 9.

Table 7: Updated dimensions of the lower skin and rear spar

	Lower skin	Rear spar
Previous thickness (mm)	4.45	2.89
Updated thickness (mm)	6.29	5.50

With these new dimensions, the highest strains are dropped from 5200 με to 3570 με as shown in Fig.47, which meets the specified design requirement. The wing tip deflection of this updated design reaches 2.4 m under limit load.

Max strain : 3570 με   Max strain : 3560 με
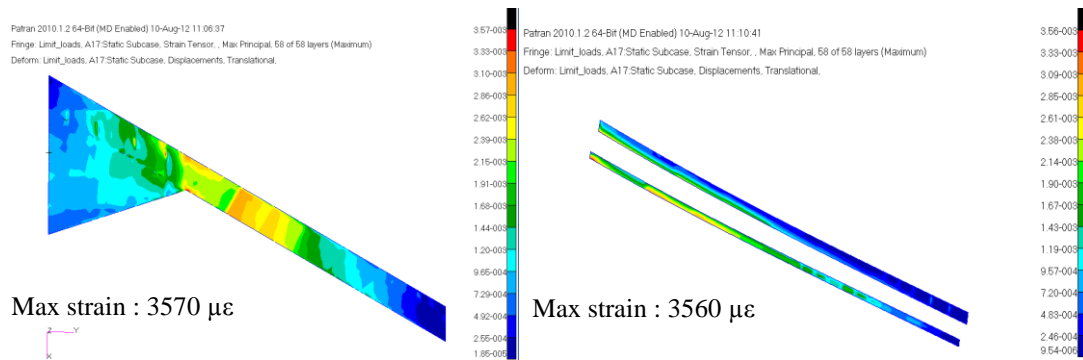
Figure 44: Strains in the lower skin and outboard rear spar (updated dimensions)

Appendix F.   Additional Gust Analysis and BDF Code in NASTRAN

F.1 Gust for sweepback shaft parallel to front spar

In this case, the shaft was set to parallel to the front spar for checking the difference in gust alleviation. It was easy to find that the efficiency of sweepback shaft configuration is not as high as the straight shaft.

Table 8 gust response with sweepback shaft PGAD

Case	Spring stiffness (Nm/rad)	Wing tip Disp. (m)	Disp. Reduction	Bending Moment (KNm)	BM Reduction	PGAD Relative Twist angle(°)
Initial design	/	3.07	/	5600	/	/
a=-0.7	5.8E4	2.81	8.5%	5195	7.2%	6.5
a=-0.5	5.8E4	2.97	3.3%	5446	2.8%	4.2

Figure 48 wing tip displacement response

Figure 49 PGAD relative twist angle
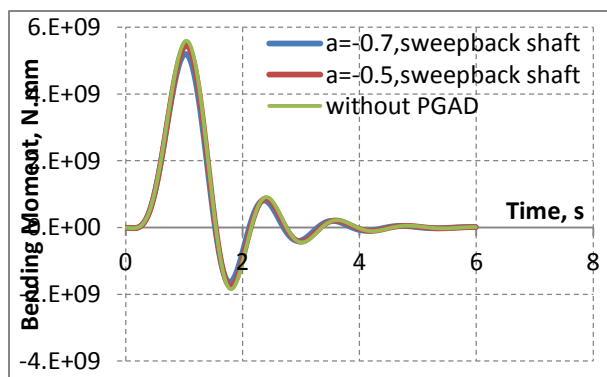
Figure 50 wing bending moment response

76

Figure 48-50 presented the analysis results in terms of wing tip displacement, PGAD relative twist angle and wing root bending moment. The device twist an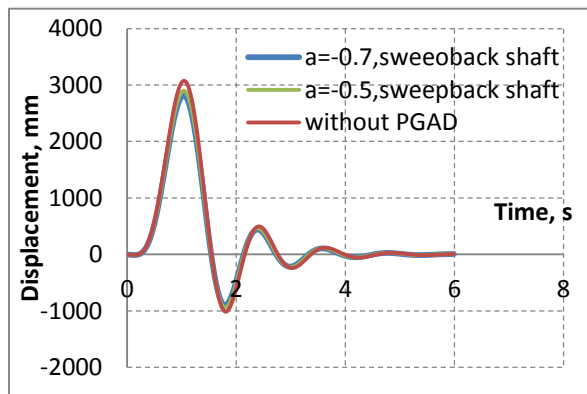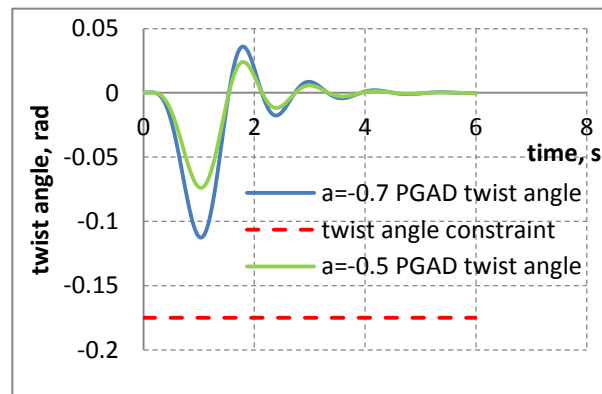gle reduced dramatically comparing with the straight shaft so that there was just a slightly alleviation about 2.8% for wing root bending moment.

The following codes are the core part of Nastran input file. Wing structure with PGAD were introduced in previous appendices in details and not included here.

F.2 BDF Code used in NASTRAN

```
$-----------------------------------Control code-------------------------------------------$
$ Dynamic Gust Analysis
SOL 146
TIME 600
CEND
$ Direct Text Input for Global Case Control Data
TITLE = MSC.Nastran Aeroelastic job created on 06-Dec-12 at 14:24:34
ECHO = NONE
MAXLINES = 999999
AECONFIG = aeroPGAD
SUBCASE 1
$ Subcase name : test
  SUBTITLE=Default
  METHOD = 1
  SDAMP = 2000         $ STRUCTURAL DAMPING (2 PERCENT)
  GUST = 1000          $ AERODYNAMIC LOADING (1-cos GUST)
  DLOAD = 1001       $ REQUIRED
  FREQ = 40        $ FREQUENCY LIST
  TSTEP = 41          $ SOLUTION TIME STEPS (1 PERIOD)
  SPC = 2

AESYMXZ = Symmetric
AESYMXY = Asymmetric
$------------------------------- GLOBAL DEFINATION --------------------------$
$ Direct Text Input for Bulk Data
PARAM   POST   0
```

77

```
PARAM   WTMASS 1.
PARAM   SNORM  20.
PARAM   PRTMAXIM YES


PARAM   GUSTAERO -1
PARAM   MACH   0.3
PARAM   Q      4.965-3


PARAM   LMODES 11
EIGRL   1              10    0
$-------------------------- GUST INFORMATION ----------------------------$
$ ID TYPE
TABDMP1 2000                                    +TABDMP
$ F1 G1 F2 G2 "ENDT"
+TABDMP 0.     .03    10.    .03    ENDT
$ SID DLOAD WG X0 V
GUST    1000   1001   0.189  -25000. 101000.0
$ SID DAREA DELAY TYPE TID
TLOAD1  1001   1002            1003
$
$ DAREA DEFINES THE DOF WHERE THE LOAD IS APPLIED AND A SCALE FACTOR.
$
$ SID P C A
DAREA   1002   90000   3     0.
TABLED1 1003                                    +TAB1
$ X1 Y1 X2 Y2 X3 Y3 X4 Y4
+TAB1   0.27692 0.02446 0.35385 0.09548 0.43076 0.20608 0.50769 0.34547 +TAB2
+TAB2   0.58462 0.49994 0.66154 0.65447 0.73846 0.79386 0.81539 0.90446 +TAB3
+TAB3   0.89231 0.97548 0.96923 1.00000 1.04615 0.97548 1.12308 0.90446 +TAB4
+TAB4   1.2     0.79381 1.27692 0.65447 1.35385 0.49994 1.43077 0.34547 +TAB5
+TAB5   1.50769 0.20608 1.58462 0.09548 1.66154 0.02446 1.73846 0       +TAB6
+TAB6   ENDT
$ SID N DT NO
FREQ1   40     0.     .125   108
TSTEP   41     600    .01    1


$---------------------------spring definition---------------------------$
$ Elements and Element Properties for region : rigidspring_ux
PELAS   108    1.+10
$ Pset: "rigidspring_ux" will be imported as: "pelas.108"
CELAS1  60000  108    90000  1     90001  1
```

78

$ Elements and Element Properties for region : rigidspring_uy

PELAS   109   1.+10

$ Pset: "rigidspring_uy" will be imported as: "pelas.109"

CELAS1 60001 109   90000 2   90001 2

$ Elements and Element Properties for region : rigidspring_uz

PELAS   110   1.+10

$ Pset: "rigidspring_uz" will be imported as: "pelas.110"

CELAS1 60002 110   90000 3   90001 3

$ Elements and Element Properties for region : rigidspring_Rx

PELAS   111   1.+10

$ Pset: "rigidspring_Rx" will be imported as: "pelas.111"

CELAS1 60003 111   90000 4   90001 4

$ Elements and Element Properties for region : rigidspring_Ry

PELAS   112   1.+7

$ Pset: "rigidspring_Ry" will be imported as: "pelas.112"

CELAS1 60004 112   90000 5   90001 5

$ Elements and Element Properties for region : rigidspring_Rz

PELAS   113   1.+10

$ Pset: "rigidspring_Rz" will be imported as: "pelas.113"

CELAS1 60005 113   90000 6   90001 6

$-------------------------------AERODYNAMICS----------------------------$

$ MKAERO2 card

$

$ Mach-Frequency Pair .MRG_MK_2

MKAERO2 .265   .2   .265   .4   .265   .6   .265   .8

MKAERO2 .265   1.   .265   1.2   .265   1.4   .265   1.6

MKAERO2 .265   1.8   .265   2.   .265   2.2   .265   2.4

MKAERO2 .265   2.6   .265   2.8   .265   3.   .265   3.2

MKAERO2 .265   3.4   .265   3.6

$

$ Aeroelastic Model Parameters

PARAM   AUNITS 1.

$

$ Global Data for Steady Aerodynamics

$

$ A half-span model is defined

$

AERO   0   90000. 6260. 1.227-12

AEROS 0   0   6260. 62280. 1.949+08

$

$ Flat Aero Surface: Device

$

PAERO1 102001

CAERO1 102001 102001 0   2   4   1

        10096. 29140.4 0.   4563. 10920. 31140. 0.   4563.

$ Flat Aero Surface: outboard_wing

$

PAERO1 101001

CAERO1 101001 101001 0   15   4   1

        -768. 10795. 0.   4563. 10096. 29140. 0.   4563.

$

$ Flat Aero Surface: inboard_wing

$

PAERO1 100001

CAERO1 100001 100001 0   5   4   1

        -7000. 0.   0.   14706. -768. 10795. 0.   4563.

$

$ Surface Spline: spline_rib_nodes_1

$

SPLINE4 1   100001 1   1   IPS   BOTH

        10   10

AELIST 1   100001 100002 100003 100004 100005 100006 100007

        100008 100009 100010 100011 100012 100013 100014 100015

        100016 100017 100018 100019 100020 101001 101002 101003

        101004 101005 101006 101007 101008 101009 101010 101011

        101012 101013 101014 101015 101016 101017 101018 101019

        101020 101021 101022 101023 101024 101025 101026 101027

        101028 101029 101030 101031 101032 101033 101034 101035

        101036 101037 101038 101039 101040 101041 101042 101043

        101044 101045 101046 101047 101048 101049 101050 101051

        101052 101053 101054 101055 101056 101057 101058 101059

        101060

SET1   1   1   4   19   43   79   123   176

        236   306   385   473   570   676   684   791

        808   913   928   1033 1048 1153 1168 1273

        1288 1393 1408 1513 1528 1633 1648 1753

        1768 1873 1888 1993 2008 2113 2128 2233

        2248 2352 2366 2477 2579 2672 2757 2833

        2899 2956 3004 3044 3078 3099 17021 17162

        17603 17872 18594 19005 19012 19504 20698 21386

SPLINE4 2   102001 2   2   IPS   BOTH

```
     10    10
AELIST 2    102001  102002  102003  102004  102005  102006  102007
     102008
SET1 2   40537  40561  40585  40743  40755  40767
```